

# Multilayer Capacitances: How Selective Contacts Affect Capacitance Measurements of Perovskite Solar Cells

Sandheep Ravishankar,<sup>1,\*</sup> Zhifa Liu,<sup>1</sup> Uwe Rau,<sup>1</sup> and Thomas Kirchartz<sup>1,2</sup>

<sup>1</sup>*IEK-5 Photovoltaik, Forschungszentrum Jülich, 52425 Jülich, Germany*

<sup>2</sup>*Faculty of Engineering and CENIDE, University of Duisburg-Essen, Carl-Benz-Str. 199, 47057 Duisburg, Germany*

 (Received 21 December 2021; revised 16 February 2022; accepted 25 February 2022; published 7 April 2022)

Capacitance measurements as a function of voltage, frequency, and temperature are a useful tool to gain a deeper insight into the electronic properties of semiconductor devices in general and of solar cells in particular. Techniques such as capacitance-voltage, Mott-Schottky analysis, or thermal-admittance spectroscopy measurements are frequently employed in perovskite solar cells to obtain relevant parameters of the perovskite absorber. However, state-of-the-art perovskite solar cells use thin electron- and hole-transport layers to improve the contact selectivity. These contacts are often quite resistive in nature, which implies that their resistance will significantly contribute to the total device impedance and thereby also affect the overall capacitance of the device, thus partly obscuring the capacitance signal from the perovskite absorber. Based on this premise, we develop a simple multilayer model that considers the perovskite solar cell as a series connection of the geometric capacitance of each layer in parallel with their voltage-dependent resistances. Analysis of this model yields fundamental limits to the resolution of spatial doping profiles and minimum values of doping and trap densities, built-in voltages, and activation energies. We observe that most of the experimental capacitance-voltage-frequency-temperature data, calculated doping and defect densities, and activation energies reported in the literature are within the derived cutoff values, indicating that the capacitance response of the perovskite solar cell is indeed strongly affected by the capacitance of its selective contacts.

DOI: [10.1103/PRXEnergy.1.013003](https://doi.org/10.1103/PRXEnergy.1.013003)

## I. INTRODUCTION

Perovskite solar cells (PSCs) have developed tremendously over the past decade, with the current highest reported efficiency for a single-junction cell standing at 25.7% [1], close to that of a single-junction crystalline silicon solar cell (26.7%) [2]. This growth has been possible largely due to structural modifications of the perovskite absorber for high-quality defect-free films that allow efficient transport of charges, combined with passivation of nonradiative recombination centers in its bulk [3–6]. Consequently, the remaining losses in state-of-the-art PSCs originate mainly from defect-mediated recombination at or close to the interfaces between the perovskite and selective contacts and also resistive losses within the selective

contacts [7–10]. Characterization of these loss mechanisms is therefore of vital importance to develop suitable design strategies to further improve the performance of state-of-the-art PSCs.

Capacitance-based techniques are frequently used for this purpose in perovskite and other emerging solar-cell technologies, to measure doping and defect densities as well as recombination coefficients or even mobilities [11]. The general idea is based on the fact that the capacitance is sensitive to the charge stored in the device. If the capacitance is measured as a function of variables such as dc bias voltage, frequency of the ac excitation, or temperature, conclusions about various important parameters can be made. For example, identification of the chemical capacitance from capacitance-voltage ( $CV$ ) measurements can provide information on the much-sought-after recombination lifetime, while the identification of the space-charge capacitance related to the existence of a depletion region in the device allows the doping density in the absorber to be calculated and spatially resolved [12]. Capacitance measurements over several orders of frequency allow the determination of the energetic depth and corresponding density of trap states, based on the characteristic frequency of the

\*s.ravi.shankar@fz-juelich.de

Published by the American Physical Society under the terms of the [Creative Commons Attribution 4.0 International license](https://creativecommons.org/licenses/by/4.0/). Further distribution of this work must maintain attribution to the author(s) and the published article's title, journal citation, and DOI.

trap [13]. This can be combined with temperature- and voltage-dependent measurements to determine the distribution of trap states both spatially and energetically in the solar cell in an apparently straightforward manner [13,14].

However, the validity and applicability of these data interpretation approaches depend on several conditions, one of which is the assumption that the capacitance of the absorber layer (in our case, the perovskite layer) either dominates the total capacitance or can be separated from other contributions to the total measured capacitance of the complete device. This is a critical and often invalid assumption because there are several different capacitances that can respond in a given measurement. The characteristic frequencies or voltage range of response of these different capacitances overlap to a certain degree, making it either extremely difficult or impossible to isolate a specific capacitive contribution that is needed for a given analysis method. Additionally, a capacitance measurement requires the measurement of a current density going into or out of the solar cell, which requires the use of contact layers. Due to the fact that metal-semiconductor interfaces are regions of high surface-recombination velocities, selective contacts or transport layers, which selectively allow for the transport of one carrier while blocking the other, are placed between the metal contacts and the absorber layer. In the case of PSCs, these transport layers are either made of metal oxides (e.g.,  $\text{TiO}_2$ ,  $\text{SnO}_2$ , or  $\text{NiO}$ ) or organic materials [e.g., poly[bis(4-phenyl)(2,4,6-trimethylphenyl)amine] (PTAA), [6, 6]-phenyl-C61-butyrac acid methyl ester (PCBM), 2,2',7,7'-tetrakis[N,N-di(4-methoxyphenyl)amino]-9,9'-spirobifluorene (Spiro-OMeTAD)]. In particular, the organic transport layers have fairly poor mobilities ( $10^{-5} - 10^{-2} \text{ cm}^2 \text{ V}^{-1} \text{ s}^{-1}$ ) [15,16] and are, therefore, fairly resistive, thin (tens of nanometers thick) layers that contribute substantially to the impedance, and therefore, the capacitance, of the device.

To unify the interpretation of the effect of the selective contacts on different capacitance methods, we develop a simple electrical model that considers the PSC as a series connection of the geometric capacitances of the perovskite and selective-contact layers, each in parallel to its voltage-dependent resistance. This extremely simple model lends itself to an analytical and comprehensive treatment that reproduces a range of nontrivial features that are frequently seen in experimental data. We complement these analytical calculations with more sophisticated numerical frequency-domain drift-diffusion simulations and compare both theoretical approaches with experimental observations from ourselves and other groups using several different capacitance methods, such as Mott-Schottky, doping profile, and thermal-admittance spectroscopy (TAS) measurements. We will show that, in all these cases, our equivalent-circuit (EC) model allows us to define a validity region of the method that depends on material and

device parameters, such as permittivities and thicknesses. In the case of Mott-Schottky or doping-profile measurements at forward bias, this leads to a fundamental limit below which the measured charge densities cannot be considered to originate from dopant or trapped charges. For charge densities below this limit, we show that the built-in voltage obtained from the Mott-Schottky plots is an artefact originating from the voltage-dependent recombination resistance of the perovskite layer, leading to a characteristic dependence on open-circuit voltage and measurement frequency. In the case of TAS measurements, the capacitance of the charge-transport layers leads to a minimum activation energy observed that depends on the built-in electrostatic potential drop over the selective-contact layers. In addition, we identify that several of these reported parameters in the literature are within the derived limits, indicating an urgent need to revise the information obtained regarding PSCs from capacitance measurements.

## II. RESULTS AND DISCUSSION

The key challenge in analyzing solar-cell capacitance measurements is unraveling the superposition of different effects that contribute to the capacitance. Any attempt to analyze data requires knowing and considering the different contributions to the capacitance. We, therefore, begin by briefly highlighting the main features of some fundamental capacitances that are observed experimentally and theoretically in solar cells (an extended discussion is provided in Sec. A1 of the Supplemental Material [17–31]). These comprise of three capacitances: the depletion capacitance, the chemical capacitance, and the diffusion capacitance. We also clarify that all capacitances referred to in this paper indicate a capacitance per unit area ( $\text{F cm}^{-2}$ ).

The depletion capacitance is associated with a space-charge region of width  $w$  in the absorber layer of thickness  $d$ , where the majority-carrier concentration is negligible with respect to the bulk. This occurs as a consequence of the electrostatic potential drop across this region due to the density of dopants or defects. This region acts as a parallel-plate capacitor, the plate spacing of which is voltage dependent, leading to its capacitance having an inverse-square-root dependence ( $C_{\text{SC}} \propto 1/\sqrt{V_{\text{BI}} - V}$ ) on the applied voltage,  $V$ , measured with respect to the built-in voltage  $V_{\text{BI}}$ . This means that a plot of  $C_{\text{SC}}^{-2}$  versus  $V$  approaches a straight line in the voltage region where the space-charge-region capacitance dominates. The plot of  $C_{\text{SC}}^{-2}$  versus  $V$  is termed a Mott-Schottky plot [32]. The slope of the Mott-Schottky region contains important information regarding the layer, such as its doping density and relative permittivity. Its intercept on the voltage axis yields the built-in electrostatic potential difference,  $V_{\text{BI}}$  [see Eq. (S3) in the Supplemental Material [17–31]]. When the absorber layer is fully depleted, the depletion

capacitance saturates to the voltage-independent geometric capacitance,  $C_g$ , of the layer.

The chemical capacitance,  $C_\mu$ , and closely related diffusion capacitance (see Secs. A1.2 and A1.3 in the Supplemental Material [17–31]), on the other hand, are related to the injection of free charge carriers into the semiconductor layer, which leads to an exponential increase in the capacitance with applied voltage ( $C \propto \exp(qV/mk_B T)$ ), where  $m$  is a dimensionless factor that we discuss in Sec. IIb. In addition to the chemical capacitance of free carriers, there also exists the chemical capacitance of trapped carriers, related to filling of the trap density of states. This capacitance makes a peak at half-occupation of the trap energy level [Eq. (S7) in the Supplemental Material [17–31]] [33]. Another contribution is from the geometric or electrode capacitances of the different layers that comprise the solar cell. In general, the response from these different capacitances can overlap, as a consequence of the similar magnitudes of the capacitances, or similar time constants that depend also on their associated resistances. Therefore, we will develop a simple electrical model of the PSC that accounts for only the fundamental mechanisms of charge injection and geometric capacitances of each individual layer of the solar cell, with the aim of identifying to which extent these factors affect or overlap with the expected response of the fundamental capacitances.

### A. Multilayer capacitances

The derivation of the fundamental capacitances described previously assumes that the contacts for charge injection and extraction are metals or thin semiconductor layers with sufficient conductivity to have very low transport resistance, i.e., to be metal-like. This means that the effective capacitance of the contacts is infinitely large, and hence, does not make any contribution to the measured capacitance of the absorber layer. However, this assumption is not valid in the case of PSCs, which frequently use thin organic layers as transport layers, the mobilities of which are low compared to those of the perovskite absorber. In such cases, the PSC cannot be considered as a capacitive perovskite layer sandwiched between two metal-like contacts, but rather as three individual layers with their own capacitances.

This approach is illustrated in Figs. 1(a) and 1(b), where the PSC is modeled as a series connection of the geometric capacitances of each layer. Each of the geometric capacitances,  $C_{g,layer}$ , is placed in parallel with its corresponding voltage-dependent resistance,  $R_{layer}$ . Such an EC model is based on the fact that, at steady state, the sum of the voltage drops across the series resistance, perovskite layer (internal voltage  $V_{int}$ ), and transport layers is equal to the external applied voltage, i.e., Ohm's law. Thus, our model can be used for the analysis of both  $n-i-p$  and  $p-i-n$  devices and represents the simplest capacitance response

of a photovoltaic device that consists of an absorber layer and corresponding low-conductivity selective contacts. As a focused point of reference, we use the parameters (see Table S2 in the Supplemental Material [17–31]) of a  $p-i-n$ -type ITO/PTAA/CH<sub>3</sub>NH<sub>3</sub>PbI<sub>3</sub>/PCBM/Ag device, as shown in Fig. 1(a). The net impedance of this system is

$$Z(V, \omega) = R_s + \left( \frac{1}{R_{PCBM}(V)} + i\omega C_{g,PCBM} \right)^{-1} + \left( \frac{1}{R_{pero}(V)} + i\omega C_{g,pero} \right)^{-1} + \left( \frac{1}{R_{PTAA}(V)} + i\omega C_{g,PTAA} \right)^{-1}. \quad (1)$$

The net capacitance is given by

$$C(V, \omega) = \frac{\text{Im}(Z^{-1})}{\omega} = \text{Im} \left[ \frac{1}{\omega} \left( R_s + \frac{R_{PCBM}(V)}{1 + i\omega R_{PCBM}(V) C_{g,PCBM}} + \frac{R_{pero}(V)}{1 + i\omega R_{pero}(V) C_{g,pero}} + \frac{R_{PTAA}(V)}{1 + i\omega R_{PTAA}(V) C_{g,PTAA}} \right)^{-1} \right]. \quad (2)$$

From Eqs. (1) and (2), we note that the impedance and, consequently, the capacitance is a function of both voltage and frequency. While the frequency dependence of the net capacitance is obvious, its voltage dependence is a consequence of the voltage-dependent resistances of one or more of the layers.

To complete the model, we require knowledge of the resistances of the individual layers as a function of voltage. In the case of the perovskite layer, we assume that it is a recombination resistance,  $R_{rec}$ , which can be easily obtained by differentiating the diode equation:

$$R_{pero} = \left( \frac{dj_{rec}}{dV_{int}} \right)^{-1} = \frac{n_{id} k_B T}{q j_0 \exp(qV_{int}/n_{id} k_B T)}, \quad (3)$$

where  $j_{rec}$  is the recombination current density,  $n_{id}$  is the ideality factor, and  $j_0$  is the reverse saturation current density.  $j_0$  can be calculated using the short-circuit current density,  $j_{sc}$ , and the open-circuit voltage:

$$j_0 = j_{sc} \exp \left( \frac{-qV_{OC}}{n_{id} k_B T} \right). \quad (4)$$

To determine the resistances of the transport layers, we first calculate the dark current through a transport layer. Figure S5 in the Supplemental Material [17–31] shows

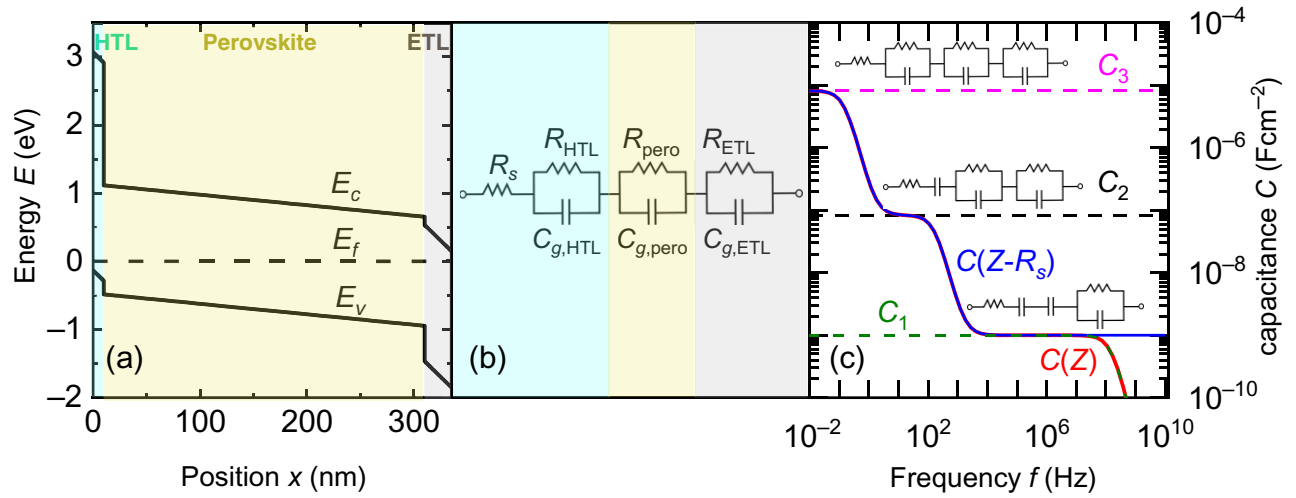


FIG. 1. (a) Band diagram of the reference PSC upon which the simulations of this paper are based (see Table S1 for parameters). (b) EC model of the solar cell in the dark.  $R_s$ ,  $R_{\text{HTL}}$ ,  $R_{\text{pero}}$ , and  $R_{\text{ETL}}$  are the series resistance and voltage-dependent resistances of the individual layers, and  $C_{g,\text{HTL}}$ ,  $C_{g,\text{pero}}$ , and  $C_{g,\text{ETL}}$  are the geometric capacitances of the individual layers. (c) Simulated capacitance evolution versus measurement frequency for the EC of (b), with ( $C(Z)$ ) and without ( $C(Z - R_s)$ ) a series resistance, for well-separated time constants of each  $R||C$  element. Three plateaus in the capacitance are observed at high frequency ( $C_1$ ), intermediate frequency ( $C_2$ ), and low frequency ( $C_3$ ), the analytical solutions of which are derived in Sec. A3 in the Supplemental Material [17–31] and shown in (c). Corresponding EC representing the capacitance plateau is shown in the inset next to each plateau. Note that the high-frequency drop in capacitance is simply a consequence of the series resistance, as derived in Sec. A3 in the Supplemental Material [17–31].

the energetics of a PSC with the absorber in contact with its respective transport layers and metal electrodes. We assume a constant Fermi-level splitting,  $V_{\text{int}}$ , in the intrinsic perovskite layer, and the difference of Fermi levels of electrons and holes at the transport layer-electrode interface is determined by the external applied voltage,  $V_{\text{ext}}$ . We also assume a constant built-in electrostatic potential  $V_{\text{BI,TL}}$  through each transport layer (i.e.,  $V_{\text{BI,ETL}}$  and  $V_{\text{BI,HTL}}$  for the electron- and hole-transport layer, respectively). The dark current through the transport layer is then given by (see Sec. A2 in the Supplemental Material [17–31] for derivation)

$$j = j_{0,\text{TL}} \left( \exp \left( \frac{qV_{\text{TL}}}{k_B T} \right) - 1 \right), \quad (5)$$

where  $j_{0,\text{TL}}$  is the dark current prefactor and  $V_{\text{TL}}$  is the potential drop across the transport layer.

The transport-layer resistance,  $R_{\text{TL}}$ , can be calculated analytically (see Sec. A2 in the Supplemental Material [17–31]) and is given by

$$R_{\text{TL}} \cong \frac{d}{q\mu n_0 \left[ \frac{q(V_{\text{BI,TL}} - V_{\text{el,TL}})}{k_B T} \right]} \left[ \exp \left( \frac{q(V_{\text{BI,TL}} - V_{\text{el,TL}})}{k_B T} \right) - 1 \right] + \frac{dk}{2q\mu n_0}, \quad (6)$$

where  $V_{\text{el,TL}}$  is the amount of the external voltage that goes to alter the electrostatic potential (controlled by parameter  $k$ ) of the transport layer,  $d$  is the thickness of the transport layer,  $\mu$  is the mobility of the majority carriers, and  $n_0$  is the majority-carrier concentration at the transport layer-electrode interface determined by the injection barrier.

Plugging the resistance in Eq. (6) into Eq. (2), we can calculate the evolution of capacitance for this model versus both voltage and frequency. We first discuss its evolution versus frequency, as shown in Fig. 1(c), to provide a basic understanding of the model.

In case of well-separated time constants of each  $R||C$  pair, we observe three capacitance plateaus, one at high frequency ( $C_1$ ), one at intermediate frequency ( $C_2$ ), and one at low frequency ( $C_3$ ). We hereafter refer to the three capacitances and their corresponding resistances using the subscripts “HF,” “IF,” and “LF,” corresponding to the magnitude of their characteristic frequencies (high, intermediate, and low frequency) and the subscripts 1–3 for the capacitance plateaus observed. The analytical equations (see Sec. A3 in the Supplemental Material [17–31] for the derivation) of the capacitance plateaus are

$$C_1 = \left[ \frac{1}{C_{\text{HF}}} \left( \frac{R_s + R_{\text{HF}}}{R_{\text{HF}}} \right)^2 + \frac{1}{C_{\text{IF}}} + \frac{1}{C_{\text{LF}}} \right]^{-1} \cong \frac{1}{C_{\text{HF}}} + \frac{1}{C_{\text{IF}}} + \frac{1}{C_{\text{LF}}}, \quad (7)$$

$$C_2 = \left[ \frac{1}{C_{LF}} + \frac{(R_s + R_{HF} + R_{IF})^2}{R_{HF}^2 C_{HF} + R_{IF}^2 C_{IF}} \right]^{-1}, \quad (8)$$

and

$$C_3 = \left[ \frac{(R_s + R_{HF} + R_{IF} + R_{LF})^2}{R_{HF}^2 C_{HF} + R_{IF}^2 C_{IF} + R_{LF}^2 C_{LF}} \right]^{-1}. \quad (9)$$

The effective EC representations of these capacitance plateaus are also shown in Fig. 1(c).

### B. Mott-Schottky plots and doping densities

One of the most important applications of capacitance measurements is the use of the Mott-Schottky plot [Eq. (S3) in the Supplemental Material [17–31]] to determine the doping density (dopants or traps) in the semiconductor layer. The doping density is calculated from the Mott-Schottky relation as

$$N_d(V) = \frac{-2(dC^{-2}/dV)^{-1}}{q\epsilon_r\epsilon_0}, \quad (10)$$

where  $N_d$  is a constant value if the Mott-Schottky region is a straight line. In the case of a spatially nonuniform doping density,  $N_d$  would slightly change with voltage. Within the framework of the depletion approximation,  $N_d(V)$  would represent the doping density at the edge of the space-charge region present at an applied voltage  $V$  [34]. Thus, to determine the doping profile, the convention is then to plot Eq. (10) versus the distance of the edge of the space-charge region to the metal contact that carries the counter charge to the charge of the majority carriers in the bulk (e.g., in a  $p$ -type semiconductor, it would be the distance to the electron-injecting contact). This distance is typically called the profiling distance (same as the space-charge

region width)  $w$ . The profiling distance follows from a simple plate-capacitor approximation of the depletion region given by

$$w(V) = \frac{\epsilon_r\epsilon_0}{C(V)}. \quad (11)$$

Note that, at sufficient reverse bias, the entire semiconductor film is fully depleted, and the measured capacitance corresponds to the geometric capacitance (assuming a dark measurement). This allows calculation of the thickness of the semiconductor layer  $d$  [see Eq. S2 in the Supplemental Material [17–31]]. The spatial resolution of the Mott-Schottky method is limited by a few Debye lengths, which reflects the fact that the majority-carrier density cannot abruptly transition from zero to the doping-density value in the neutral zone at the edge of the depletion layer [34]. In addition, in the case of PSCs, the measurement frequency must be chosen carefully to avoid capacitive contributions from the mobile ions within the perovskite layer. Capacitance measurements on thin-film devices have identified that ionic effects occur at frequencies of  $10^3$  Hz and below [35–39]. Therefore, for capacitance measurements, we expect that frequencies above these values will be sufficient to neglect ionic contributions to the spectra. However, conductivity measurements on perovskite pellets and films have identified ionic transport frequencies of  $10^5$  Hz and below [40,41]. The discrepancies between these measured ionic transport times are not clearly understood yet. Finally, the measurement of the capacitance itself is limited by the measurement system's ability to resolve the phase angle ( $\sim 0.5^\circ$  for our Zahner system), which can significantly affect the validity of data at large forward bias and low frequencies (see Fig. S7 in the Supplemental Material [17–31]).

Figure 2(a) shows some experimentally measured capacitance-voltage plots under dark conditions and

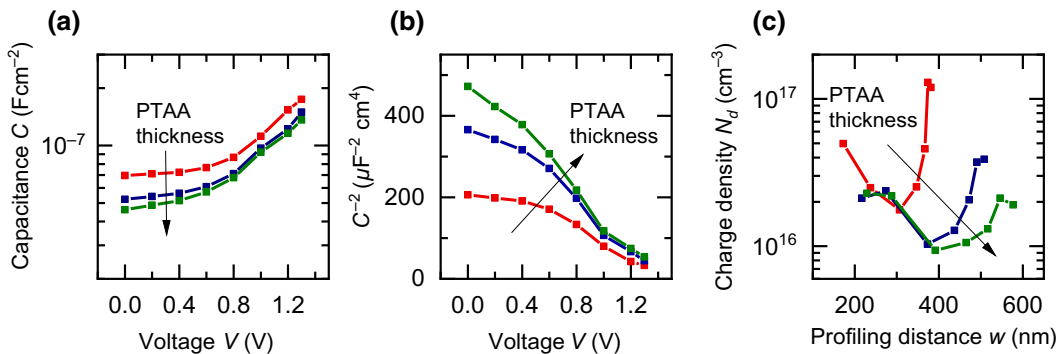


FIG. 2. Experimentally measured (a) capacitance versus voltage plots, (b) Mott-Schottky plots, and (c) doping profiles for ITO/PTAA/ $\text{CH}_3\text{NH}_3\text{Pb}(\text{I}_{0.8}\text{Br}_{0.2})_3/\text{PCBM}/\text{BCP}/\text{Ag}$  samples with increasing thickness of the PTAA layer, as indicated in the inset. Fits of the capacitance versus voltage to the equation  $C = C_g + C_0 \exp(qV/mk_B T)$  to obtain the  $m$  value are shown in Fig. S8(a) in the Supplemental Material [17–31]. Measurement frequency is 25 469 Hz.

Figs. 2(b) and 2(c) show the corresponding Mott-Schottky and doping-profile plots, respectively, for ITO/PTAA/CH<sub>3</sub>NH<sub>3</sub>Pb(I<sub>0.8</sub>Br<sub>0.2</sub>)<sub>3</sub>/PCBM/BCP (Bathocuproine)/Ag samples [42] (see the Supplemental Material [17–31] for information on fabrication) with increasing thickness of the PTAA layer. The measurement frequency of 25 469 Hz is chosen because it corresponds to the high-frequency plateau in the capacitance, which should be related to the free-carrier response. The capacitance-voltage profiles show a weak exponential increase of the capacitance starting at around 0.5 V with slope factor  $m$  between 12.7 and 16.4 [see Fig. S8(a) in the Supplemental Material for fits], making it difficult to identify its mechanistic origin. The corresponding Mott-Schottky plots also show the onset of the linear Mott-Schottky region at intermediate forward bias, around 0.4 V for all the samples.

A summary of Mott-Schottky plots of different PSCs reported in literature are shown in Fig. 3(a). The nature of

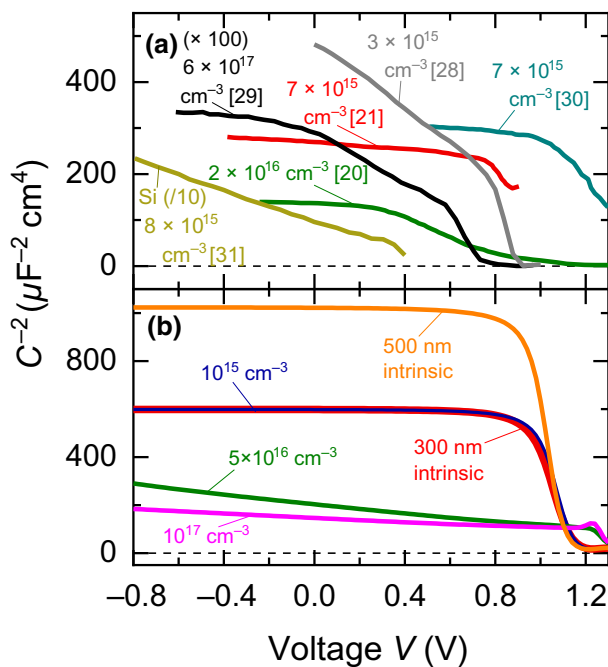


FIG. 3. (a) Mott-Schottky plots of different PSCs and a silicon solar cell reported in the literature. Corresponding calculated doping densities are shown in the label, obtained from their corresponding doping profiles [see Fig. S8(b) in the Supplemental Material [17–31]]. (b) Simulated Mott-Schottky plots of a PSC with different acceptor doping densities of the perovskite layer, as shown in the label, using SCAPS. Orange and red lines are simulations of an intrinsic perovskite layer with different thicknesses. Simulated Mott-Schottky plots for an intrinsic layer and dopant density of  $10^{15} \text{ cm}^{-3}$  are very similar to each other and to the experimental plots shown in (a). Literature data are obtained from refs. [35,36,43–46], as mentioned in the corresponding label.

these plots is very similar to that of Fig. 2(b), showing the linear Mott-Schottky region only at intermediate-to-large forward bias with either a plateau or weak evolution at lower voltages. In addition, we can also observe a second linear region with reduced slope (downward kink) at large forward bias in some of the plots, which is generally assigned to a contribution from the exponential chemical or ionic capacitance [43,44]. Literature data suggest doping densities in the perovskite layer [calculated from their corresponding doping profiles, see Fig. S8(b) in the Supplemental Material [17–31]] between  $3 \times 10^{15}$  and  $7 \times 10^{17} \text{ cm}^{-3}$ . As a reference, a Mott-Schottky plot of a monocrystalline silicon solar cell is also shown in Fig. 3(a), which shows a similar doping density to the perovskite data points but a very different Mott-Schottky plot, yielding a clear linear Mott-Schottky region from deep reverse bias to forward bias. SCAPS simulations of PSCs with different doping densities shown in Fig. 3(b) also indicate that the onset of the Mott-Schottky region should occur from deep reverse bias, while, conversely, for doping densities of about  $10^{15} \text{ cm}^{-3}$ , the behavior is identical to that of an intrinsic perovskite. Furthermore, the expected onset voltage,  $V_{\text{onset}}$ , of the space-charge capacitance is plotted as a function of doping density and perovskite layer thickness in Fig. 4(a), calculated by setting the space-charge capacitance equal to the geometric capacitance of the perovskite layer. For typical thin-film PSCs of thickness 300 nm, doping densities in excess of approximately  $3 \times 10^{16} \text{ cm}^{-3}$  should show an onset of the Mott-Schottky plot at reverse bias, which is not observed in literature data in Fig. 3(a). However, for lower reported doping densities, the onset voltage coincides with that observed in literature data, i.e., intermediate-to-large forward bias. Therefore, based on the analysis so far, it is still difficult to confirm the validity of the doping densities reported in the literature from the Mott-Schottky analysis of PSCs.

However, Ref. [47] has previously discussed the sensitivity of the Mott-Schottky analysis for organic solar cells, identifying that, in cases where the doping density is not high enough to alter the bulk carrier concentration sufficiently to create a neutral region, an apparent Mott-Schottky plot similar to the one generated by an intrinsic perovskite shown in Fig. 3(b) is obtained. This apparent Mott-Schottky region can originate from either the chemical capacitance or from transitions between the geometric capacitances of the different layers comprising the solar cell, based on the model developed in Sec. IIa (see Fig. S9 in the Supplemental Material [17–31]). This is because the resistances in this model depend exponentially on the external voltage, and hence, the capacitance also shows an exponential evolution with the external voltage [see Eqs. (2), (3), and (6)]. To account for the effects of these two additional voltage-dependent capacitances that can create an apparent Mott-Schottky region, we define the general

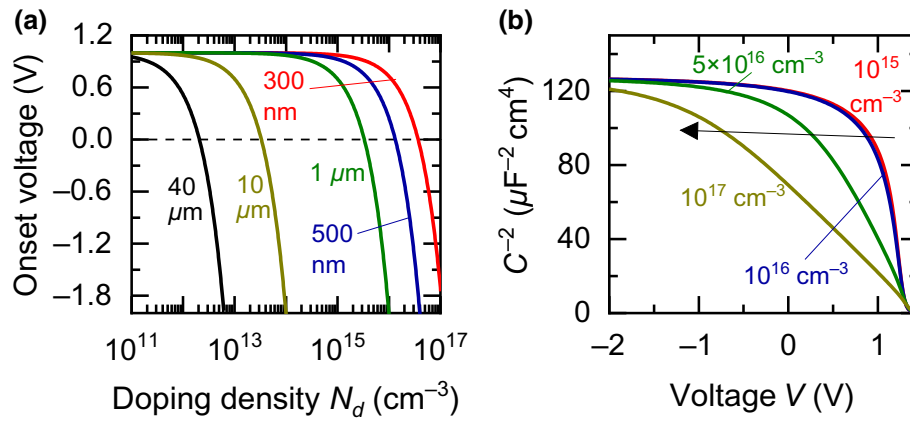


FIG. 4. (a) Onset voltage of the space-charge capacitance as a function of doping density for different thicknesses of the absorber layer, calculated by setting the space-charge capacitance [Eq. (S1) in the Supplemental Material [17–31]] equal to the geometric capacitance. For thin-film solar cells, dopant densities in excess of  $10^{16} \text{cm}^{-3}$  are required to observe the space-charge capacitance at reverse bias. (b) SCAPS simulations of Mott-Schottky plots of a PSC (without selective contacts and 0-eV injection barrier on either side) with different doping densities of the perovskite layer, as shown in the label. Arrow indicates the shift in the onset voltage of the linear Mott-Schottky region with increasing doping density.

voltage-dependent capacitance as

$$C(V) = C_g + C_0 \exp\left(\frac{qV}{mk_B T}\right), \quad (12)$$

where  $C_g$  is the geometric capacitance,  $C_0$  is a prefactor, and  $m$  is a parameter that controls the slope of the exponential evolution of the capacitance versus voltage. Carrying out a Mott-Schottky analysis of Eq. (12) using Eq. (10) (see Sec. A4 and A5 in the Supplemental Material [17–31] for the derivation), we obtain a charge density given by [48]

$$N_{d,\min} = \frac{27mk_B T \epsilon_r \epsilon_0}{4q^2 d_{\text{pero}}^2}. \quad (13)$$

Equation (13) provides a lower limit of resolution and suggests that only charge densities that are significantly above this limit can be considered as originating from doping or trap densities in capacitance measurements. For commonly used perovskite layer thicknesses between 300 and 1000 nm, we obtain apparent doping densities between  $6 \times 10^{15}$  and  $2 \times 10^{14} \text{cm}^{-3}$ , assuming  $m = 1$ . The large values of  $m$  observed experimentally ( $m > 10$ , see Fig. S8 in the Supplemental Material [17–31]) then suggest that this limit increases by at least an order of magnitude to  $6 \times 10^{16} \text{cm}^{-3}$  for a 300-nm-thick perovskite layer and  $2 \times 10^{15} \text{cm}^{-3}$  for a 1000-nm-thick perovskite layer. These charge densities are very similar to the measured doping densities seen in Fig. 3(a), suggesting that the calculated doping densities are erroneous and in fact originate from the response of the chemical capacitance or geometric capacitances, rather than from a depletion-layer capacitance. In addition, Eq. (13) implies that, for measured

charge densities close to the resolution limit, thin films will always show higher apparent doping or trap densities compared to a bulk single crystal due to the inverse-square-thickness dependence. Therefore, care must be taken during such measurements, since such a trend is intuitively expected based on the higher crystallinity of bulk single crystals compared to thin films.

We now justify the use of Eq. (12) to represent the capacitance-voltage evolution of the multilayer model developed in Sec. IIa. Figure 5(a) shows the simulated capacitance evolution of this model versus applied voltage, and Fig. 5(b) shows the corresponding Mott-Schottky plot. The capacitance remains flat through most of the voltage range before it starts to increase exponentially and peaks at a certain value. This creates a Mott-Schottky plot very similar to those observed in Fig. 3(a). To understand how the constant geometric capacitances of the PSC can make a step in the capacitance versus voltage, we must look at the evolution of the characteristic frequencies of the layers and their corresponding resistances. The characteristic frequencies are given by

$$\omega_{\text{layer}}(V) = [R_{\text{layer}}(V)C_{\text{layer}}]^{-1}, \quad (14)$$

where the “layer” subscript indicates the name of the different layers comprising the solar cell. The voltage dependence of the resistances of the PTAA, perovskite, and PCBM layers [see Eqs. (3) and (6)] causes their corresponding characteristic frequencies to evolve with voltage, both of which are plotted in Figs. 5(c) and 5(d), respectively. The resistance of the perovskite layer decreases exponentially with applied forward bias because it is a recombination resistance, while the contact-layer resistances show an exponential decrease with applied forward

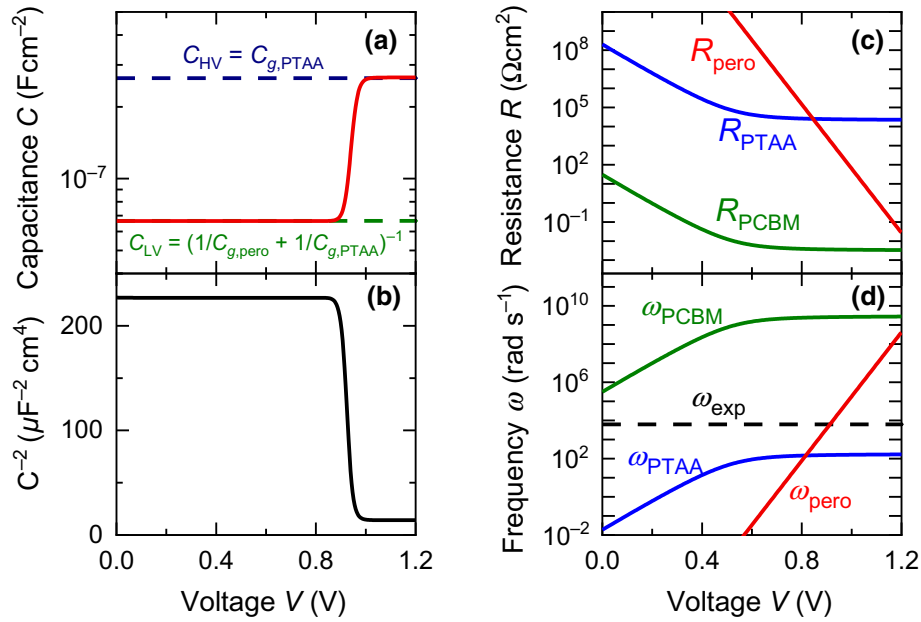


FIG. 5. Simulated evolution of (a) capacitance, (b) corresponding Mott-Schottky plot, (c) resistances, and (d) characteristic frequencies versus applied voltage based on the multilayer model developed in Sec. IIa.  $V_{\text{int}} \cong V_{\text{ext}}$  is assumed in these simulations, which is a good approximation for the relevant voltage range in dark measurements [see fig. S6(a) in the Supplemental Material [17–31]]. Parameters are discussed in Table S2 in the Supplemental Material [17–31]. Green and blue dashed lines in (a) correspond to the low-voltage capacitance limit,  $C_{\text{LV}}$ , and high-voltage capacitance limit,  $C_{\text{HV}}$  [Eqs. (S50) and (S52) in the Supplemental Material [17–31]]. Measurement frequency is chosen to be  $f_{\text{exp}} = 10^3$  Hz.

bias related to increasing conductivity upon injection of majority carriers and saturates at a minimum value,  $R_{\text{TL,min}}$  [see Eq. (S37) in the Supplemental Material [17–31]]. By comparing the values of the characteristic frequencies to the measurement frequency,  $\omega_{\text{exp}}$ , we can derive analytical approximations (see Sec. A3 in the Supplemental Material [17–31]) of the low- and high-voltage plateaus of capacitance ( $C_{\text{LV}}$  and  $C_{\text{HV}}$ , respectively) in Fig. 5(a) as

$$C_{\text{LV}} = \left( \frac{1}{C_{\text{PTAA}}} + \frac{1}{C_{\text{perov}}} \right)^{-1}, \quad (15)$$

$$C_{\text{HV}} = C_{\text{PTAA}}, \quad (16)$$

with the principle being that only those capacitances with characteristic frequencies that are much smaller than the measurement frequency dominate the net capacitance. The low-voltage plateau is then the series connection of the geometric capacitances of the PTAA and perovskite layers, which transitions to a high-voltage plateau of the geometric capacitance of the PTAA layer. Comparing the Mott-Schottky behavior of the multilayer model with that of the depletion capacitance and the chemical capacitance shows that their behavior is very similar and overlaps at the same voltage range, with only reverse-bias conditions being suitable to clearly isolate the response of the depletion capacitance (see Fig. S9 in the Supplemental Material [17–31]).

Therefore, to discriminate such effects from actual Mott-Schottky behavior arising from a depletion-layer capacitance, we must ensure the calculated doping densities are significantly higher than Eq. (13). Additionally, we note that, in any working solar cell, there has to be some amount of charge injection, and hence, a contribution from the chemical capacitance to the total capacitance (which might be hidden, as is the case for PSCs). This suggests that the capacitance evolution of the PSC is likely a combination of the chemical-capacitance and multilayer-geometric-capacitance transition mechanisms, both of which evolve exponentially, as previously discussed. Simulations including the chemical capacitance in the multilayer-capacitance model are shown in Fig. S10 in the Supplemental Material [17–31]. Larger  $m$  values alter the plateau at low voltages, creating a weak evolution in the apparent Mott-Schottky region, similar to that observed experimentally in Fig. 3(a). Note that the downward kink at large forward bias seen in the Mott-Schottky plots in Fig. 3(a) is also reproduced in this model.

### C. The relationship between the open-circuit voltage and built-in voltage

Another important parameter that is obtained from Mott-Schottky plots (intercept on the voltage axis) is the built-in electrostatic potential drop,  $V_{\text{BI}}$  (generally referred to as the

built-in voltage), in the absorber layer. The built-in voltage is generated upon equilibration of the Fermi levels of the metallic and semiconductor layers in the device and, depending on the doping density, can drop in a small layer at an interface, as is the case for strongly doped crystalline silicon solar cells, or drop across the entire thickness of the absorber for an intrinsic solar cell. In general, the built-in voltage is important to maximize the performance of a solar cell, offering the beneficial properties of charge selectivity and preventing the formation of extraction barriers for electrons and holes at large forward biases. For intrinsic low-mobility semiconductors, the  $V_{\text{BI}}$  also allows efficient charge separation and transport under short-circuit conditions while also reducing recombination under open-circuit conditions by reducing the density of minority carriers at either interface [49,50].

Therefore, it is intuitively expected that larger  $V_{\text{BI}}$  values will result in higher open-circuit voltages. This is indeed observed from experimental Mott-Schottky data reported in the literature, shown in Fig. 6(a). These data points correspond to cases where the improved performance and open-circuit voltage of a passivated sample compared to an unpassivated sample is interpreted as occurring due to efficient charge extraction as a consequence of the increased  $V_{\text{BI}}$  observed for the passivated sample from the Mott-Schottky plot. However, the exact mechanism regarding how passivation alters the equilibrium electrostatic potential distribution is unclear. To confirm the validity of this interpretation, we simulate the effect of variations in open-circuit voltage using the multilayer model because the recombination resistance in the model creates an open-circuit voltage dependence [Eqs. (3) and (4)]. Figure 6(b) shows the simulated Mott-Schottky plots, which show the same trend of increased apparent  $V_{\text{BI}}$  with increasing open-circuit voltage, as observed experimentally in Fig. 6(a). An

analytical equation showing the open-circuit voltage and frequency dependence of the capacitance step that yields the apparent  $V_{\text{BI}}$  from the multilayer model is provided in Sec. A7 in the Supplemental Material [17–31] [Eq. (S79)].

We can conclude that, in situations where the Mott-Schottky transition does not arise from a depletion capacitance, the observed  $V_{\text{BI}}$  is only an artefact generated by a step in the capacitance. Therefore, any increase in the open-circuit voltage due to passivation or material modification causes an increase in the apparent  $V_{\text{BI}}$  and not the other way around. This occurs due to the fundamental dependence of the recombination resistance of the perovskite layer on its open-circuit voltage in combination with charge injection or multilayer-capacitance transitions. Arguments of increased charge extraction due to an apparent increased  $V_{\text{BI}}$  from Mott-Schottky plots, therefore, cannot be invoked to justify an increase in the open-circuit voltage of passivated samples compared to unpassivated ones.

#### D. Interpretation of doping profiles

We now turn to understanding the spatial dependence of the apparent doping density from doping-profile plots. Figure 2(c) shows the measured doping profiles of ITO/PTAA/ $\text{CH}_3\text{NH}_3\text{Pb}(\text{I}_{0.8}\text{Br}_{0.2})_3$ /PCBM/BCP/Ag solar cells for different thicknesses of the PTAA layer. The doping profile makes a “U” shape, with a plateau region in the apparent bulk of the perovskite layer and steep rises at both small and large apparent profiling distances corresponding to regions close to the interfaces of the perovskite with the selective contacts. This U shape moves to lower charge densities and larger profiling distances for increasing thickness of the PTAA layer. Such a doping profile and its evolution with PTAA-layer thickness is intuitively puzzling; however, based on our previous

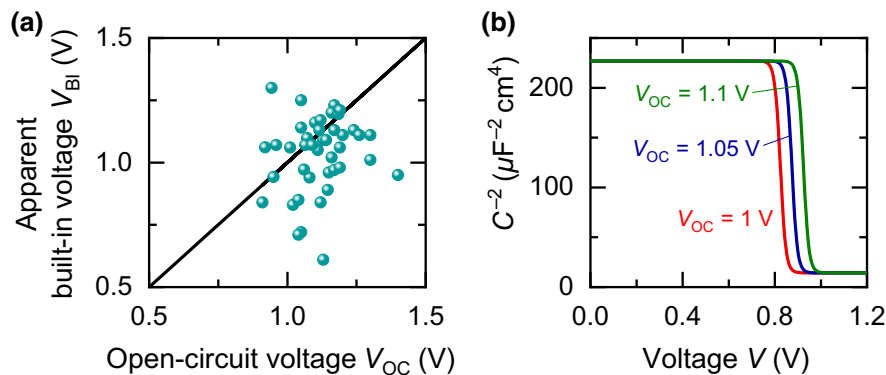


FIG. 6. (a) Plot of reported apparent built-in voltages obtained from Mott-Schottky analysis in the literature versus corresponding open-circuit voltages. Solid line indicates the region where  $V_{\text{BI}} = V_{\text{OC}}$ . Larger built-in voltages are associated with larger open-circuit voltages. (b) Simulated Mott-Schottky plots for different open-circuit voltages shown in the label, using the multilayer model. Measurement frequency is chosen to be  $f_{\text{exp}} = 10^3$  Hz. Multilayer model predicts the trend observed in (a) for the evolution of built-in voltage versus open-circuit voltage. Literature data correspond to Refs. [36,43–45,51–67]. Variation of the built-in voltage of the multilayer model as a function of frequency is shown in Fig. S13(b) in the Supplemental Material [17–31].

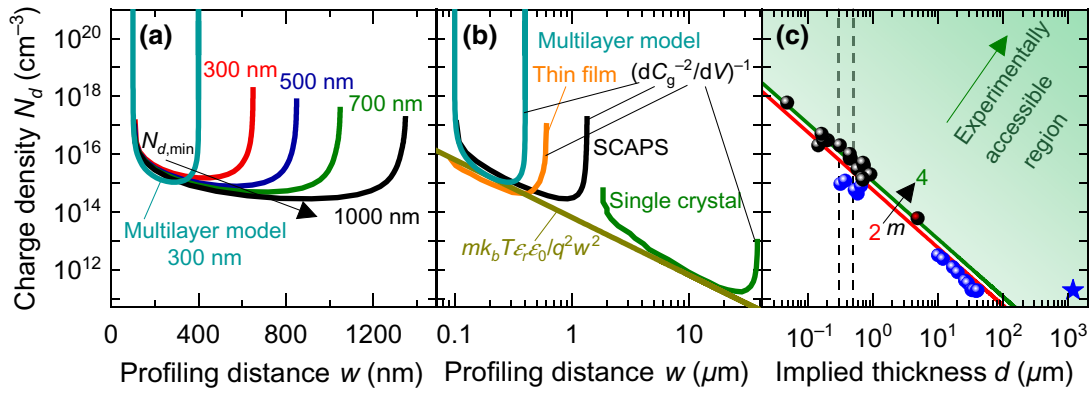


FIG. 7. (a) Simulated spatial doping profiles (from *CV* simulations) of a thin-film PSC for different thicknesses of the perovskite layer, using SCAPS and the multilayer model developed in Sec. IIa. Arrow indicates the reduction of the minimum doping density obtained in the plateau region, versus perovskite-layer thickness. (b) Comparison of experimental (from Ref. [68]) and simulated spatial doping profiles for different PSCs. Analytical approximation of the forward-bias behavior of the doping profile, as predicted by Eq. (17) ( $m = 1.5$  is assumed), is also shown. Slopes of experimental data match nicely with this limit. (c) Comparison of minimum doping density resolvable from capacitance measurements and calculated minimum doping densities (lowest value of plateau region of doping profile) versus implied perovskite-layer thickness from different capacitance measurements of PSCs. Blue data points correspond to DLCP measurements in Ref. [68]. Black data points correspond to *CV* measurements in Refs. [35,36,43–45,61,66,67,69,70], where the implied perovskite-layer thickness is calculated using Eq. (S2) in the Supplemental Material [17–31] (the validity of which is assumed during a Mott-Schottky analysis) with  $\epsilon_r = 30$  from the low-bias saturation-capacitance value. Black dotted lines indicate the typical thin-film perovskite-layer thicknesses used. Area between the red and green lines sets the range of the limiting doping-density value, depending on the  $m$  value of the capacitance transition. PSCs generally show large  $m$  values, see Fig. S8(a) in the Supplemental Material [17–31]. Star indicates the only data point (from Ref. [68]) that lies above the resolution limit and the black point filled with red indicates a device without selective contacts [70].

analysis of the Mott-Schottky plots, we speculate that this profile is generated by the combination of the multilayer model and the chemical capacitance. To confirm our hypothesis, we carry out SCAPS simulations of spatial doping profiles of thin-film trap-free dopant-free PSCs with different thicknesses of perovskite layer, shown in Fig. 7(a).

All the profiles form the U shape observed in Fig. 2(c), even in the absence of any traps or dopant densities. The simulated apparent charge densities of a PSC with 300 nm thickness of the perovskite layer is similar in magnitude to the experimental values seen in Fig. 2(c). Furthermore, an analysis of the doping profiles of several different photovoltaic technologies shows that they all yield the same U shape [48], which would be quite a coincidental occurrence. These observations suggest that these apparent charge densities are indeed related to signals from the chemical capacitance and the multilayer model. We, therefore, derive analytical approximations (see Secs. A4 and A5 in the Supplemental Material [17–31]) of the doping profile by considering a simple geometric capacitance in parallel to a general capacitance that evolves exponentially with voltage, as carried out previously [Eq. (13)]. Since the doping profile is determined by the inverse slope of the Mott-Schottky plot [Eq. (10)], the rise in apparent charge density at large profiling distances (reverse bias) is simply due to the constant geometric capacitance. The plateau region in the doping profile thus corresponds to

the apparent linear Mott-Schottky region in the bulk of the sample (intermediate forward bias), yielding a minimum doping-density value. For small profiling distances (large forward bias), we observe another sharp rise in doping density, corresponding to the plateau region at large forward bias of the Mott-Schottky plot. The plateau region and forward-bias rise of the doping profile can be analytically calculated as [48]

$$N_d(w) = N_{d,min} + \frac{mk_B T \epsilon_r \epsilon_0}{q^2 w^2}, \quad (17)$$

where  $N_{d,min}$  is the minimum charge density shown in Eq. (13). A simulated doping profile using the multilayer model is also shown in Fig. 7(a), which shows a very similar behavior to the SCAPS simulations, lending further credence to our developed model. There are also some other interesting observations to be made. Equations (13) and (17) predict a reduction in the bulk doping density (plateau region of U shape) of these profiles with increasing thickness of the perovskite layer, due to the inverse square dependence of  $N_{d,min}$  on the layer thickness  $d$ , as seen in Fig. 7(a). Additionally, we note that the apparent profiling distances in Fig. 7(a) and experimental data of Fig. 2(c) extend to distances larger than the thickness of the perovskite layer. This is further confirmation of the contribution of capacitances that are not related to the depletion-layer capacitance, causing either an error in the

values of capacitance or the choice of relative permittivity. We will now proceed to further interpret experimental data based on the previous analysis after a short discussion on measurement methods of these doping profiles.

Recently, Ni *et al.* [68] used drive-level capacitance profiling (DLCP) to spatially resolve apparent trap densities in the PSC. DLCP is a similar technique to standard  $CV$  measurements but also uses a first-order term in voltage in addition to the zero-order term that gives the standard  $CV$  response [71]. The general charge response,  $Q$ , in a capacitance measurement is given by the Taylor expansion:

$$Q(\bar{V} + \tilde{V}) = Q(\bar{V}) + \frac{d\bar{Q}}{d\bar{V}}\tilde{V} + \left(\frac{d^2\bar{Q}}{2d\bar{V}^2}\right)\tilde{V}^2 + \dots, \quad (18)$$

where overbars represent steady-state quantities, and the tilde represents a time-dependent quantity. Equation (18) can be rearranged to give the capacitance as

$$C = \frac{d\bar{Q}}{d\bar{V}} = C_0 + C_1\tilde{V} + \dots \quad (19)$$

The first term on the right-hand side of Eq. (19) corresponds to the zero-order capacitance term measured from  $CV$ , while the second term is included in case of a DLCP measurement. Therefore, any differences between the DLCP and  $CV$  responses arise from the frequency or voltage dependence of the first-order term's coefficient. This term is shown to have a weak frequency dependence in PSCs and is then used to differentiate between the free and trapped charge responses going from high to low frequencies [68]. Using this assumption, Ni *et al.* identified a U-shaped profile for both the trap and doping densities for different PSCs. We have shown previously that such an interpretation is incorrect and that Eq. (13) is still valid for all measurement frequencies [48]. Therefore, experimental doping profiles obtained from DLCP measurements will hereafter be shown in conjunction with  $CV$  simulations to obtain a unified and consistent interpretation.

Figure 7(b) shows a comparison of experimental doping profiles obtained from DLCP measurements of both a perovskite thin film and bulk single crystal, in conjunction with a  $CV$  simulation of a dopant-free trap-free PSC and a simulated doping profile from the multilayer model. The typical U shape of the experimental doping profile and the reduction in apparent bulk doping density with increasing thickness is clearly observed in this figure. For small profiling distances (forward bias), Fig. 7(b) illustrates clearly that the experimental and simulated data follow the predicted  $w^{-2}$  dependence of the apparent doping densities in Eq. (17). Figure 7(c) summarizes the minimum doping densities obtained from capacitance-voltage (black)

and DLCP (blue) measurements reported in the literature and compared to the minimum doping-density limit,  $N_{d,\min}$ , derived [Eq. (13)] for different implied thicknesses of the perovskite layer [calculated from the saturation of the capacitance at low forward bias, see Eq. (S2) in the Supplemental Material [17–31]]. This limit is plotted for different  $m$  values, depending on the type of capacitance that dominates the capacitance step (see Fig. S9 in the Supplemental Material [17–31]). The DLCP data points all lie just below the  $m = 2$  line for both thin films and bulk single crystals, while the data points from  $CV$  measurements lie close to the  $m = 4$  line. Only one data point lies clearly in the green region, well above the resolution limit, a perovskite single crystal measured by Ni *et al.* [68] Apart from this data point, all the other data points correspond to complete devices with transport layers and, therefore, we conclude that the transport-layer capacitances dominate the capacitance step at forward bias. In addition, Fig. 7(c) contains one data point (black point filled with red) that corresponds to a PSC without selective contacts (ITO/CH<sub>3</sub>NH<sub>3</sub>PbBr<sub>3</sub>/Au), measured by Peng *et al.* [70]. This data point also lies very close to the resolution limit and is experimental evidence of a situation where the chemical capacitance dominates the capacitance step. Further proof of the invalidity of the measured doping and defect densities in PSCs using capacitance methods is provided by the fact that the measured lifetimes show no correlation to the device thickness [unlike the apparent defect densities, which clearly show a  $d^{-2}$  trend from Fig. 7(c)] [72]. We also note that a significant displacement along the  $x$  axis is also observed for some of the Mott-Schottky data when compared to typical thin-film thicknesses used [shown using black dashed lines in Fig. 7(c)], where the implied perovskite-layer thickness is estimated from the saturation of the capacitance at the lowest bias point. This is related to the fact that the experimentally observed capacitance plateau at low forward biases does not directly correspond to the geometric capacitance of the perovskite layer [see Figs. 5(a) and 5(b)] and related errors in the assumed permittivity.

In summary, the application of the traditional Mott-Schottky method to obtain doping densities and the built-in potential in the PSC is complicated by the concomitant contributions of the transport-layer geometric capacitances and the chemical capacitance of the perovskite layer to the total measured capacitance at forward bias. Therefore, depending on the  $m$  value of the multilayer-chemical capacitance transition, only charge densities significantly higher than  $N_{d,\min}$  for the given thickness of the perovskite layer can be considered to originate from any real doping or trapped charge densities [green region in Fig. 7(c)]. Our analysis of experimental doping profiles from the literature and our own samples indicates that the calculated doping and trap densities of PSCs using capacitance-voltage methods are below the limit of resolution provided by

the fundamental response of a trap-free dopant-free intrinsic perovskite layer. We recommend that any calculated doping and defect densities from capacitance-voltage measurements must first be compared to the resolution limit provided in Eq. (13). If it is significantly higher than this value, it can safely be reported as a doping or defect density. If it is below or close to this resolution limit, it can only be considered as an upper limit to the actual doping and defect density in the device. Second, the onset of the linear Mott-Schottky region in a Mott-Schottky plot can be compared to the theoretical onset voltage for the calculated doping density, shown in Fig. 4(a), as an additional validity check.

We also emphasize that the model and analysis methods developed are applicable to any solar cell that consists of an absorber layer and low-conductivity selective contacts. Thus, the multilayer model must be considered as the simplest or base response of a range of photovoltaic technologies, as discussed for Cu(In,Ga)Se<sub>2</sub> solar cells [73,74]. Furthermore, the model is applicable to a wide range of device configurations and is independent of the constituents or performance of the device, assuming that hysteresis effects are not significant enough to prevent stable and reproducible capacitance spectra from being obtained. The model can also be extended to electron- or hole-transport-layer-free devices by setting the mobility of the omitted layer infinitely high. The developed resolution limit in Eq. (13) is also independent of the device configuration and performance and depends only on the geometric capacitance and the slope of the exponential capacitance step that occurs.

### E. Capacitance plateaus: Evolution versus frequency

In this section, we will attempt to shed some light on the mechanisms governing the frequency-dependent evolution of the dark capacitance of the PSC. In a system that consists of several different capacitances, we expect to observe several plateaus and corresponding transitions from one net capacitance to the other with a sweep of the measurement frequency. There are a number of candidate capacitances that can cause these plateaus, which are discussed in the introduction of Sec. II. These include the chemical capacitance, depletion capacitance, trap capacitance, and the geometric capacitances of the individual layers of the solar cell. In the case of PSCs, we also have a capacitance response from mobile ions in the bulk and accumulated ions at interfaces [39]. The timescales for the responses of these capacitances (which also depend on the resistances they are coupled with) usually overlap, at least to a certain degree, making it quite difficult to identify which capacitance is responding in a given measurement.

The capacitance evolution versus frequency of an ITO/PTAA/CH<sub>3</sub>NH<sub>3</sub>Pb(I<sub>0.8</sub>Br<sub>0.2</sub>)<sub>3</sub>/PCBM/BCP/Ag PSC for different applied voltages is shown in Fig. 8(a). At low

forward biases, we observe a single plateau at high frequencies, the magnitude of which increases with applied voltage, followed by a small step in the capacitance, starting at about 10<sup>3</sup> Hz, as shown in Fig. 8(b). At large forward bias, we additionally observe a low-frequency capacitance that overshadows the small capacitance step at intermediate frequencies with a magnitude that is very large, in the order of millifarads per cm<sup>2</sup>. This low-frequency capacitance and its evolution with voltage and light intensity have been extensively investigated and associated with the density of mobile ions within the PSC (see Fig. S11 in the Supplemental Material [17–31]), although the exact mechanism is debated [75–79]. The interpretation of this low-frequency capacitance is further affected by inconsistency in measurements due to time drift in the response of the PSC at low frequencies, for which correction procedures have been suggested [80]. The interpretation of ionic effects in the capacitance response is out of the scope of this work; therefore, we will focus on the interpretation of the high- and intermediate-frequency capacitance behavior. However, this does not imply that the multilayer model is not relevant for the analysis of low-frequency data of PSCs. As stated in Sec. IID, the multilayer model provides the simplest capacitance response of a solar cell that consists of an absorber layer and selective-contact layers. Therefore, any experimental capacitance steps that are assigned to ionic effects that can be sufficiently reproduced by the multilayer model (that does not consider ionic effects) must be questioned as to the interpretation of its origin. To explicitly account for ionic effects, the multilayer model can be extended by the addition of a resistor in series with a capacitor, in parallel to the perovskite R||C element [40,78]. This resistance corresponds to a transport resistance for mobile ions across the perovskite bulk terminating in an ionic capacitance, where the ions accumulate at the blocking interfaces to form double layers. Accumulation of electronic charges at these interfaces due to the electrostatic potential drop created by the ions can also lead to increased recombination at these locations, which can be modeled by an additional recombination resistance in parallel to the ionic accumulation capacitance [75]. Advanced modeling of the ionic diffusion behavior can be carried out by using a transmission line [81]. Similar assumptions of ionic accumulation at interfaces and subsequent drift or diffusion are used to model the ionic response in time-domain capacitance measurements [35]. However, we note that the exact modeling of the ionic response is an open question due to the complexity of the ionic-electronic interaction in the PSC [39].

To understand if the complex capacitance-frequency-voltage behavior in Fig. 8(a) can originate from the simple geometric capacitance transitions of the multilayer model, we carry out simulations of a dopant-free trap-free PSC using both SCAPS and the multilayer model, as shown in Figs. 8(c) and 8(d), respectively. For SCAPS simulations,

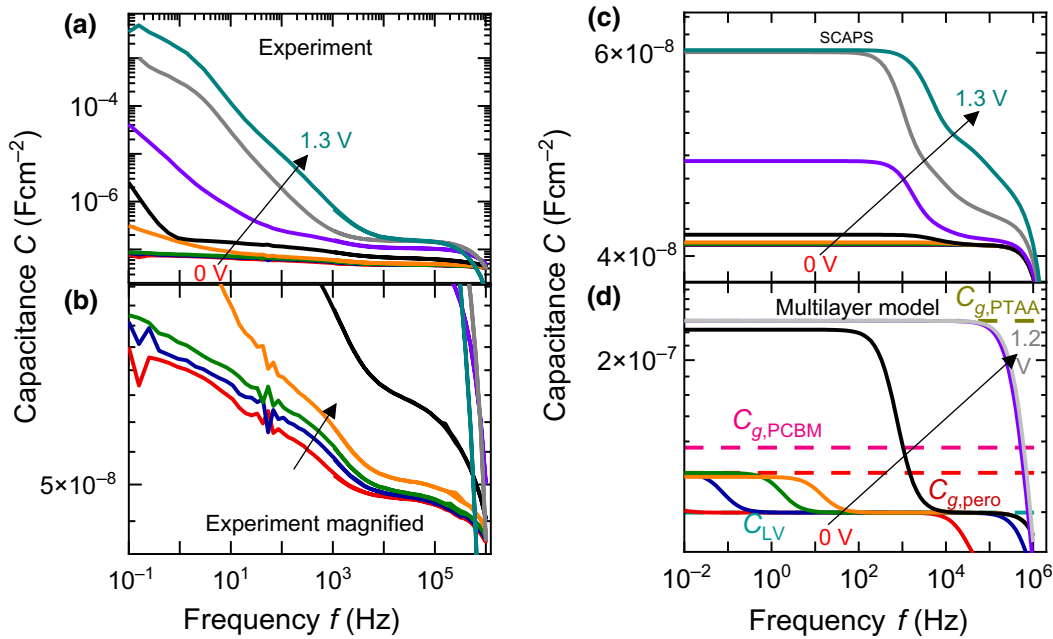


FIG. 8. (a) Experimental dark capacitance evolution versus frequency for different applied voltages for an ITO/PTAA/CH<sub>3</sub>NH<sub>3</sub>Pb(I<sub>0.8</sub>Br<sub>0.2</sub>)<sub>3</sub>/PCBM/BCP/Ag PSC. (b) is a magnified plot of (a), showing an additional capacitance step (indicated by the arrow) at frequencies between 10<sup>-1</sup> and 10<sup>4</sup> Hz at low forward biases. (c) SCAPS simulations of the capacitance-voltage-frequency behavior of a PSC [band diagram in Fig. 1(a)]. Mobilities of the PCBM and PTAA layers are set to  $\mu = 10^{-6}$  cm<sup>2</sup>V<sup>-1</sup>s<sup>-1</sup> in (c). (d) Simulations of the capacitance-voltage-frequency behavior from the multilayer model.  $C_{LV}$  corresponds to the low-voltage capacitance plateau of Eq. (S50) in the Supplemental Material [17–31]. Multilayer model reproduces the general capacitance features observed in experiments versus applied voltage and frequency. Steep rise in capacitance at low frequencies seen in (a) is related to the mobile ionic density in the PSC, which are not included in the simulations of (c) and (d).

the mobilities of both the selective contacts are set at  $\mu = 10^{-6}$  cm<sup>2</sup>V<sup>-1</sup>s<sup>-1</sup> to increase the resistance of the contact layers sufficiently. The SCAPS simulations show similar behavior to the experimentally measured data, showing two capacitance plateaus at high and intermediate frequencies, the magnitudes of which both increase with applied voltage. Simulations using the multilayer model also generate behavior similar to the experimentally observed transitions with voltage and frequency (excluding the ionic capacitance transition at large forward bias and low frequency), with a high-frequency capacitance step, the magnitude of which increases with applied forward voltage followed by a small low-frequency (between about 10<sup>0</sup> and 10<sup>2</sup> Hz) step observed at only low forward voltages. Additionally, we note that the high-frequency drop-off in capacitance [ $> 10^5$  Hz in Figs. 8(a), 8(c), and 8(d)] is a consequence of the series resistance [see Fig. 1(c)] and should not be mistaken as originating from the trapping and detrapping of electronic charges [82]. Therefore, we can conclude that the multilayer-capacitance model, which is based on transitions between the geometric capacitances of the resistive selective-contact layers and the absorber layer, is a credible model that can reproduce the general electronic-carrier-related features of the capacitance-voltage-frequency behavior of the PSC.

## F. Thermal-admittance spectroscopy (TAS)

Thermal-admittance spectroscopy is a technique that aims to obtain information regarding the depth and density of trap states within the semiconductor band gap by identifying the trap's contribution to the measured capacitance, through the variation of temperature and frequency. It has been widely used for the characterization of different semiconductor technologies [83–87]. The method relies on the fact that the trapping and detrapping processes occur on a characteristic timescale. This means that, upon the application of a small ac voltage perturbation, the trapping-detrapping processes can either follow the modulation of the Fermi level or not, depending upon the frequency employed. This leads to a frequency-dependent capacitance response from the trapped charges, which can be combined with its fundamental temperature dependence to obtain the depth of the trap within the band gap using the following relationship [13]:

$$\ln\left(\frac{\omega_{\text{inf}}}{T^2}\right) = \ln k - \frac{E_A}{k_B T}, \quad (20)$$

where  $\omega_{\text{inf}}$  is the inflection frequency of the capacitance transition;  $T$  is the temperature in Kelvin;  $k$  is a constant; and  $E_A$  is the demarcation or activation energy, which is

the depth of the trap energy level from the conduction or valence band. Based on Eq. (20), admittance measurements are made over a range of frequencies as a function of temperature, usually at zero voltage bias. From the inflection points of the capacitance versus frequency,  $\omega_{\text{inf}}$  for each temperature point is determined and the slope of ( $\omega_{\text{inf}}/T^2$ ) versus  $1/k_B T$  yields the activation energy.

Before examining experimental data reported in the literature, we will first examine the TAS response of our multilayer model. To determine  $\omega_{\text{inf}}$  of the multilayer model, we consider two  $R||C$  elements in series, yielding a transition from a high-frequency capacitance plateau to a low-frequency capacitance plateau, as shown in Sec. A6 in the Supplemental Material [17–31]. The inflection frequency is then calculated as (see Sec. A8 in the Supplemental Material [17–31])

$$\omega_{\text{inf}} \propto \frac{1}{k_B T} \exp \left[ -\frac{q(V_{\text{BI,TL}} - V_{\text{el,TL}})}{k_B T} \right]. \quad (21)$$

Since TAS measurements are usually carried out at zero-bias conditions, we then have the apparent activation energy from the multilayer model:

$$E_A = qV_{\text{BI,TL}} - 3k_B T. \quad (22)$$

Simulated capacitance measurements versus frequency as a function of temperature for the multilayer model are shown in Fig. 9(a). We observe three plateaus, one at low temperature, followed by a transition to the second capacitance plateau at higher frequencies for increasing

temperatures, while the third plateau occurs at low frequencies below 100 Hz. The transition region for all these plateaus shifts to higher frequencies for increasing temperatures. Similar capacitance-frequency-temperature trends have been observed experimentally for the PSC. For  $n-i-p$  devices, two capacitance steps are generally observed from TAS measurements: one that originates at 300 K at high frequencies ( $\sim 10^5 - 10^6$  Hz), termed  $D1$ , and one that originates at 300 K at low frequencies ( $\sim 10^2 - 10^3$  Hz), termed  $D2$  [88–94]. The origin of these capacitance steps could be electronic, ionic (measured ionic transport frequencies from conductivity measurements on perovskite pellets and films are  $\sim 10^5$  Hz and below [40,41]), or a combination of both. However, since the  $D1$  step is a few orders faster than the  $D2$  step, we consider it to be more strongly influenced by electronic effects (trapping-detrapping), and hence, focus on its analysis. We again emphasize that though our model does not include ionic effects; it is still valid in frequency ranges where the ions apparently dominate the capacitance to clearly discriminate the ionic response from the expected electronic response of the absorber and transport layers.

Figure 9(b) shows the TAS response of the “ $D1$ ” step reported in the literature for different PSCs. A large dispersion in the apparent activation energies, ranging from 20 to 200 meV, is calculated from these plots. The corresponding TAS response and calculated activation energies from the multilayer model for different built-in voltages of the PCBM layer are also shown (dashed lines). We note that the dominant resistance for the  $D1$  transition in the

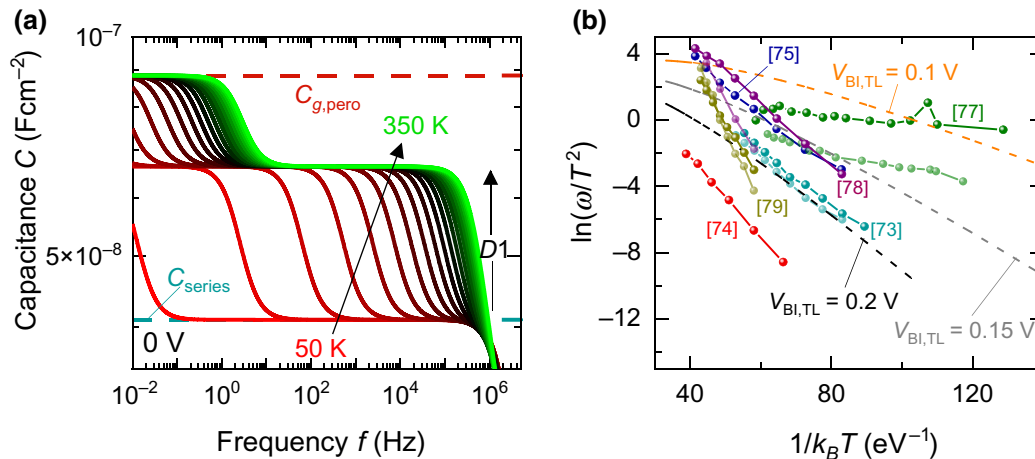


FIG. 9. (a) Simulated evolution of capacitance versus frequency for different temperatures using the multilayer model.  $D1$  step generally observed for  $n-i-p$  PSCs at high frequencies is labeled. (b) Comparison of TAS data reported in the literature for PSCs with simulated TAS results using the multilayer model (dashed) for the  $D1$  step using different built-in voltages,  $V_{\text{BI,TL}}$ , for the electron-transport layer. Literature data are obtained from refs. [88–93], as mentioned in the corresponding label. Fits of simulated activation energies to the analytical solution in Eq. (22) are shown in Fig. S14 in the Supplemental Material [17–31]. Experimental data sets from the same literature reference are shown in light and dark colors. Electron-transport-layer mobility is reduced to  $2 \times 10^{-3} \text{ cm}^2 \text{ V}^{-1} \text{ s}^{-1}$  for the simulations in (a) and (b), while  $V_{\text{BI,ETL}} = V_{\text{BI,HTL}} = 0.1$  V is used for (a).

multilayer model is the electron-transport-layer resistance due to the large characteristic frequency of its corresponding  $R||C$  element at zero bias, see Fig. 5(d). Therefore, we expect the built-in voltage of the electron-transport layer to affect the TAS behavior of the  $D1$  step, the values of which are hence varied.

The simulated evolution from the multilayer model is similar to experimental data, making a straight line at lower temperatures (large  $1/k_B T$ ) and slightly curving downwards at higher temperatures (small  $1/k_B T$ ) due to the temperature-dependent term in Eq. (22) [fits of simulated data using analytical Eq. (22) shown in Fig. S14 in the Supplemental Material [17–31]]. The corresponding apparent activation energies obtained for reasonable values of  $V_{BI}$  of the electron-transport layer are well within the range of commonly measured activation energies for the PSC, as seen from the slopes of the plots in Fig. 9(b). This indicates that several of the experimental TAS data observed do not arise from the trapping and detrapping of free charge carriers in the perovskite layer. Instead, they are likely an artefact caused by the contribution of the capacitances and resistances of the selective contacts. Similar conclusions were made from TAS measurements on PSCs with and without the selective contacts by Awani *et al.* [88], who suggested that the  $D1$  capacitance step and associated activation energy commonly measured was actually a response from trapping-detrapping processes in the hole-selective-contact layer.

The problem in interpreting TAS data becomes clear when considering Eqs. (12) in Ref. [13] and (S76) in the Supplemental Material [17–31], which correspond to the frequency dependence of the trap capacitance and the capacitance associated with a general  $R||C$  transition, respectively. Both these capacitances possess an inverse-square-frequency dependence, and hence, show very similar evolution versus frequency. Therefore, the geometric capacitance transitions arising from the multilayer model must be considered as a lower limit to the measured activation energies of not only PSCs but any photovoltaic technology that makes use of additional nonmetallic layers (selective contacts) in the device stack. The limit itself is determined by the electrostatic potential drop through the selective contact, the resistance of which dominates the capacitance transition in the frequency and temperature range of interest.

### III. CONCLUSIONS

We carry out a critical assessment of various commonly used capacitance techniques to probe perovskite solar cells. These include  $CV$ , Mott-Schottky analysis, drive-level capacitance profiling, and TAS measurements, which, in principle, yield information on key parameters, such as spatial and energetic distributions of doping and trap densities. However, the use of selective contacts in

these devices, which are often quite resistive in nature, means that these layers possess impedances with signals that can overlap with those from the perovskite layer. We explain this phenomenon by the development of a simple multilayer model that considers the perovskite solar cell as a series connection of the geometric capacitances of the selective contacts and the perovskite layer, with each capacitance in parallel with its transport or recombination resistance. The voltage dependence of these resistances, and hence, the characteristic frequencies of each layer, create a rich capacitance-voltage-frequency-temperature behavior that is, in several cases, similar to that observed experimentally. The model is adaptable for any configuration of the device and is independent of the composition of the absorber layer. Thus, despite its simplicity, the multilayer model serves as a base model for the capacitance response of not only perovskite solar cells but any photovoltaic technology that consists of an absorber layer and low-conductivity selective contacts, creating fundamental limits below which the observed response cannot be considered as originating from fundamental mechanisms such as doping, trap, or chemical capacitances.

In the case of Mott-Schottky measurements, such an analysis leads to a minimum doping and trap density that has an inverse dependence on the thickness of the absorber layer. At this limit, polycrystalline thin-film solar cells will show larger apparent trap and doping densities compared to bulk single-crystal devices, which can be misconstrued as a valid result, as it is intuitively expected. The multilayer model also yields a fundamental dependence of the apparent built-in voltages obtained from Mott-Schottky plots on the open-circuit voltage and measurement frequency, the evolution of which is similar to that observed experimentally [45,52,61]. This means that commonly used arguments of better charge collection due to an increased built-in voltage observed from Mott-Schottky plots upon passivation or material modification are incorrect, rather it is the higher open-circuit voltage that causes an increase in the apparent built-in voltage observed. Additionally, the model also predicts a typical U shape of the spatial doping profile, yielding a constant, minimum doping or trap density in the bulk with large increases of the doping or trap densities over several orders near the perovskite-selective-contact interfaces that is also observed experimentally [68]. These large peaks in doping and trap densities are simply a consequence of the constant geometric capacitance at reverse bias and geometric capacitance transitions coupled with charge injection at forward bias. Finally, in the case of TAS measurements, we show that the trap-induced capacitance-frequency transition has a similar form to any arbitrary capacitance-frequency transition between  $R||C$  elements in series. This yields an apparent activation energy that depends on the built-in electrostatic potential drop through the selective-contact layer that dominates the transition, which must be considered as a cutoff

value for the calculated trap-activation energies from this method.

The calculated minimum-resolution values for all these capacitance methods show a significant overlap with several experimental data sets in the literature, indicating that the capacitance response of the perovskite solar cell is indeed strongly affected by its resistive contact layers.

Scripts for all simulations in this paper are archived in Zenodo [95].

## ACKNOWLEDGMENTS

S.R. acknowledges the German Research Foundation (DFG) for support through a Walter-Benjamin fellowship Project No. 462572437. U.R. and T.K. acknowledge funding from the Helmholtz Association via the project PER-OSEED. Open access publication funded by the German Research Foundation (DFG) Grant No. 491111487.

S.R. carried out all the experiments, simulations, calculations, and wrote the manuscript. Z.L. fabricated the samples. U.R. contributed to deriving the transport-layer resistance and reviewing the manuscript. T.K. conceptualized and supervised the project and contributed to reviewing and editing the manuscript.

There are no conflicts of interest to declare.

- 
- [1] M. Kim, J. Jeong, H. Lu, T. K. Lee, F. T. Eickemeyer, Y. Liu, I. W. Choi, S. J. Choi, Y. Jo, H.-B. Kim, *et al.*, Conformal quantum dot-SnO<sub>2</sub> layers as electron transporters for efficient perovskite solar cells, *Science* **375**, 302 (2022).
- [2] K. Yoshikawa, H. Kawasaki, W. Yoshida, T. Irie, K. Konishi, K. Nakano, T. Uto, D. Adachi, M. Kanematsu, H. Uzu, *et al.*, Silicon heterojunction solar cell with interdigitated back contacts for a photoconversion efficiency over 26%, *Nat. Energy* **2**, 17032 (2017).
- [3] M. Saliba, T. Matsui, J. Seo, K. Domanski, J.-P. Correa-Baena, M. K. Nazeeruddin, S. M. Zakeeruddin, W. Tress, A. Abate, and A. Hagfeldt, Cesium-containing triple cation perovskite solar cells: Improved stability, reproducibility and high efficiency, *Energy Environ. Sci.* **9**, 1989 (2016).
- [4] M. Saliba, T. Matsui, K. Domanski, J.-Y. Seo, A. Ummadisingu, S. M. Zakeeruddin, J.-P. Correa-Baena, W. Tress, A. Abate, and A. Hagfeldt, Incorporation of rubidium cations into perovskite solar cells improves photovoltaic performance, *Science* **354**, 206 (2016).
- [5] M. Abdi-Jalebi, Z. Andaji-Garmaroudi, S. Cacovich, C. Stavrakas, B. Philippe, J. M. Richter, M. Alsari, E. P. Booker, E. M. Hutter, and A. J. Pearson, Maximizing and stabilizing luminescence from halide perovskites with potassium passivation, *Nature* **555**, 497 (2018).
- [6] F. Gao, Y. Zhao, X. Zhang, and J. You, Recent progresses on defect passivation toward efficient perovskite solar cells, *Adv. Energy Mater.* **10**, 1902650 (2020).
- [7] M. Stolterfoht, C. M. Wolff, J. A. Marquez, S. Zhang, C. J. Hages, D. Rothhardt, S. Albrecht, P. L. Burn, P. Meredith, and T. Unold, Visualization and suppression of interfacial recombination for high-efficiency large-area pin perovskite solar cells, *Nat. Energy* **3**, 847 (2018).
- [8] M. Stolterfoht, P. Caprioglio, C. M. Wolff, J. A. Marquez, J. Nordmann, S. Zhang, D. Rothhardt, U. Hörmann, Y. Amir, and A. Redinger, The impact of energy alignment and interfacial recombination on the internal and external open-circuit voltage of perovskite solar cells, *Energy Environ. Sci.* **12**, 2778 (2019).
- [9] C. M. Wolff, P. Caprioglio, M. Stolterfoht, and D. Neher, Nonradiative recombination in perovskite solar cells: The role of interfaces, *Adv. Mater.* **31**, 1902762 (2019).
- [10] I. L. Braly, D. W. deQuilettes, L. M. Pazos-Outón, S. Burke, M. E. Ziffer, D. S. Ginger, and H. W. Hillhouse, Hybrid perovskite films approaching the radiative limit with over 90% photoluminescence quantum efficiency, *Nat. Photonics* **12**, 355 (2018).
- [11] M. T. Khan, M. Salado, A. Almohammadi, S. Kazim, and S. Ahmad, Elucidating the impact of charge selective contact in halide perovskite through impedance spectroscopy, *Adv. Mater. Interfaces* **6**, 1901193 (2019).
- [12] J. Bisquert, *The Physics of Solar Energy Conversion: Perovskites, Organics, and Photovoltaic Fundamentals* (CRC Press, Boca Raton, 2020). Ch.7, 9.
- [13] T. Walter, R. Herberholz, C. Müller, and H. Schock, Determination of defect distributions from admittance measurements and application to Cu(In, Ga)Se<sub>2</sub> based heterojunctions, *J. Appl. Phys.* **80**, 4411 (1996).
- [14] J. T. Heath, J. D. Cohen, and W. N. Shafarman, Bulk and metastable defects in CuIn<sub>1-x</sub>Ga<sub>x</sub>Se<sub>2</sub> thin films using drive-level capacitance profiling, *J. Appl. Phys.* **95**, 1000 (2004).
- [15] E. Von Hauff, V. Dyakonov, and J. Parisi, Study of field effect mobility in PCBM films and P3HT: PCBM blends, *Sol. Energy Mater. Sol. Cells* **87**, 149 (2005).
- [16] S. Barard, M. Heeney, L. Chen, M. Cölle, M. Shkunov, I. McCulloch, N. Stingelin, M. Philips, and T. Kreouzis, Separate charge transport pathways determined by the time of flight method in bimodal polytriarylamine, *J. Appl. Phys.* **105**, 013701 (2009).
- [17] See Supplemental Materials at <http://link.aps.org/supplemental/10.1103/PRXEnergy.1.013003> for experimental and simulation methods, discussion of simulation parameters, description of fundamental capacitances in solar cells, derivation of transport-layer resistance, analytical approximations of capacitance plateaus, derivation of analytical resolution limit and doping profile at forward bias, description of general R||C capacitance transition, and the derivation of the apparent activation energy of a general R||C transition. The following references [18–31] are also included in the Supplemental Materials.
- [18] M. Burgelman, P. Nollet, and S. Degraeve, Modelling polycrystalline semiconductor solar cells, *Thin Solid Films* **361**, 527 (2000).
- [19] S. Sami, P. A. Haase, R. Alessandri, R. Broer, and R. W. Havenith, Can the dielectric constant of fullerene derivatives be enhanced by side-chain manipulation? A predictive first-principles computational study, *J. Phys. Chem. A* **122**, 3919 (2018).
- [20] M. Sendner, P. K. Nayak, D. A. Egger, S. Beck, C. Müller, B. Epping, W. Kowalsky, L. Kronik, H. J. Snaith, A. Pucci, *et al.*, Optical phonons in methylammonium lead halide

- perovskites and implications for charge transport, *Mater. Horiz.* **3**, 613 (2016).
- [21] Z. Liu, L. Krückemeier, B. Krogmeier, B. Klingebiel, J. A. Márquez, S. Levchenko, S. Öz, S. Mathur, U. Rau, T. Unold, *et al.*, Open-circuit voltages exceeding 1.26 V in planar methylammonium lead iodide perovskite solar cells, *ACS Energy Lett.* **4**, 110 (2018).
- [22] J. Maibach, E. Mankel, T. Mayer, and W. Jaegermann, *J. Mater. Chem. C* **1**, 7635 (2013).
- [23] A. Magomedov, A. Al-Ashouri, E. Kasparavičius, S. Strazdaite, G. Niaura, M. Jošt, T. Malinauskas, S. Albrecht, and V. Getautis, Self-assembled hole transporting monolayer for highly efficient perovskite solar cells, *Adv. Energy Mater.* **8**, 1801892 (2018).
- [24] S. Cook, R. Katoh, and A. Furube, Ultrafast studies of charge generation in PCBM: P3HT blend films following excitation of the fullerene PCBM, *J. Phys. Chem. C* **113**, 2547 (2009).
- [25] Y. Kim, S. A. Choulis, J. Nelson, D. D. Bradley, S. Cook, and J. R. Durrant, Composition and annealing effects in polythiophene/fullerene solar cells, *J. Mater. Sci.* **40**, 1371 (2005).
- [26] F. Staub, H. Hempel, J.-C. Hebig, J. Mock, U. W. Paetzold, U. Rau, T. Unold, and T. Kirchartz, Beyond Bulk Lifetimes: Insights Into Lead Halide Perovskite Films From Time-Resolved Photoluminescence, *Phys. Rev. Appl.* **6**, 044017 (2016).
- [27] L. M. Herz, Charge-Carrier mobilities in metal halide perovskites: Fundamental mechanisms and limits, *ACS Energy Lett.* **2**, 1539 (2017).
- [28] M. Büttiker, H. Thomas, and A. Prêtre, Mesoscopic capacitors, *Phys. Lett. A* **180**, 364 (1993).
- [29] J. Bisquert, Chemical capacitance of nanostructured semiconductors: Its origin and significance for nanocomposite solar cells, *Phys. Chem. Chem. Phys.* **5**, 5360 (2003).
- [30] W. Shockley and W. Read Jr, Statistics of the recombinations of holes and electrons, *Phys. Rev.* **87**, 835 (1952).
- [31] A. Neugroschel, Determination of lifetimes and recombination currents in pn junction solar cells, diodes, and transistors, *IEEE Trans. Electron Devices* **28**, 108 (1981).
- [32] S. M. Sze and K. K. Ng, *Physics of Semiconductor Devices* (John Wiley & Sons, New York, 2006), Ch. 2.
- [33] J. Bisquert, Theory of the impedance of charge transfer via surface states in dye-sensitized solar cells, *J. Electroanal. Chem.* **646**, 43 (2010).
- [34] W. C. Johnson and P. T. Panousis, The influence of debye length on the CV measurement of doping profiles, *IEEE Trans. Electron Devices* **18**, 965 (1971).
- [35] M. H. Futscher, M. K. Gangishetty, D. N. Congreve, and B. Ehrler, Quantifying mobile ions and electronic defects in perovskite-based devices with temperature-dependent capacitance measurements: Frequency vs time domain, *J. Chem. Phys.* **152**, 044202 (2020).
- [36] S. Reichert, J. Flemming, Q. An, Y. Vaynzof, J.-F. Pietschmann, and C. Deibel, Ionic-Defect Distribution Revealed by Improved Evaluation of Deep-Level Transient Spectroscopy on Perovskite Solar Cells, *Phys. Rev. Appl.* **13**, 034018 (2020).
- [37] S. Reichert, Q. An, Y.-W. Woo, A. Walsh, Y. Vaynzof, and C. Deibel, Probing the ionic defect landscape in halide perovskite solar cells, *Nat. Commun.* **11**, 1 (2020).
- [38] S. Tammireddy, S. Reichert, Q. An, A. D. Taylor, R. Ji, F. Paulus, Y. Vaynzof, and C. Deibel, Temperature-dependent ionic conductivity and properties of iodine-related defects in metal halide perovskites, *ACS Energy Lett.* **7**, 310 (2022).
- [39] H. Wang, A. Guerrero, A. Bou, A. M. Al-Mayouf, and J. Bisquert, Kinetic and material properties of interfaces governing slow response and long timescale phenomena in perovskite solar cells, *Energy Environ. Sci.* **12**, 2054 (2019).
- [40] T. Y. Yang, G. Gregori, N. Pellet, M. Grätzel, and J. Maier, The significance of Ion conduction in a hybrid organic-inorganic lead-iodide-based perovskite photosensitizer, *Angew. Chem.* **127**, 8016 (2015).
- [41] D. V. Amasev, V. G. Mikhalevich, A. R. Tameev, S. R. Saitov, and A. G. Kazanskii, Formation of a two-phase structure in  $\text{CH}_3\text{NH}_3\text{PbI}_3$  organometallic perovskite, *Semiconductors* **54**, 654 (2020).
- [42] Z. Liu, J. Siekmann, B. Klingebiel, U. Rau, and T. Kirchartz, Interface optimization via fullerene blends enables open-circuit voltages of 1.35V in  $\text{CH}_3\text{NH}_3\text{Pb}(\text{I}_{0.8}\text{Br}_{0.2})_3$  solar cells, *Adv. Energy Mater.* **11**, 2003386 (2021).
- [43] M. Fischer, K. Tvingstedt, A. Baumann, and V. Dyakonov, Doping profile in planar hybrid perovskite solar cells identifying mobile ions, *ACS Appl. Energy Mater.* **1**, 5129 (2018).
- [44] O. Almora, C. Aranda, E. Mas-Marzá, and G. Garcia-Belmonte, On Mott-Schottky analysis interpretation of capacitance measurements in organometal perovskite solar cells, *Appl. Phys. Lett.* **109**, 173903 (2016).
- [45] A. Zohar, M. Kulbak, I. Levine, G. Hodes, A. Kahn, and D. Cahen, What limits the open-circuit voltage of bromide perovskite-based solar cells?, *ACS Energy Lett.* **4**, 1 (2018).
- [46] O. Almora, L. G. Gerling, C. Voz, R. Alcubilla, J. Puigdollers, and G. Garcia-Belmonte, Superior performance of  $\text{V}_2\text{O}_5$  as hole selective contact over other transition metal oxides in silicon heterojunction solar cells, *Sol. Energy Mater. Sol. Cells* **168**, 221 (2017).
- [47] T. Kirchartz, W. Gong, S. A. Hawks, T. Agostinelli, R. C. MacKenzie, Y. Yang, and J. Nelson, Sensitivity of the Mott-Schottky analysis in organic solar cells, *J. Phys. Chem. C* **116**, 7672 (2012).
- [48] S. Ravishankar, T. Unold, and T. Kirchartz, Comment on “Resolving spatial and energetic distributions of trap states in metal halide perovskite solar cells”, *Science* **371**, eabd8014 (2021).
- [49] T. Kirchartz, J. Bisquert, I. Mora-Sero, and G. Garcia-Belmonte, Classification of solar cells according to mechanisms of charge separation and charge collection, *Phys. Chem. Chem. Phys.* **17**, 4007 (2015).
- [50] U. Rau and T. Kirchartz, Charge carrier collection and contact selectivity in solar cells, *Adv. Mater. Interfaces* **6**, 1900252 (2019).
- [51] X. Gong, Q. Sun, S. Liu, P. Liao, Y. Shen, C. Grätzel, S. M. Zakeeruddin, M. Grätzel, and M. Wang, Highly efficient perovskite solar cells with gradient bilayer electron transport materials, *Nano Lett.* **18**, 3969 (2018).
- [52] J.-H. Lee, J. Kim, G. Kim, D. Shin, S. Y. Jeong, J. Lee, S. Hong, J. W. Choi, C.-L. Lee, and H. Kim, Introducing paired electric dipole layers for efficient and reproducible

- perovskite solar cells, *Energy Environ. Sci.* **11**, 1742 (2018).
- [53] D. B. Khadka, Y. Shirai, M. Yanagida, T. Noda, and K. Miyano, Tailoring the open-circuit voltage deficit of wide-band-gap perovskite solar cells using alkyl chain-substituted fullerene derivatives, *ACS Appl. Mater. Interfaces* **10**, 22074 (2018).
- [54] Y. Chen, X. Zuo, Y. He, F. Qian, S. Zuo, Y. Zhang, L. Liang, Z. Chen, K. Zhao, and Z. Liu, Dual passivation of perovskite and SnO<sub>2</sub> for high-efficiency MAPbI<sub>3</sub> perovskite solar cells, *Adv. Sci.* **8**, 2001466 (2021).
- [55] K. Choi, J. Lee, H. I. Kim, C. W. Park, G.-W. Kim, H. Choi, S. Park, S. A. Park, and T. Park, Thermally stable, planar hybrid perovskite solar cells with high efficiency, *Energy Environ. Sci.* **11**, 3238 (2018).
- [56] C. Dong, X. Han, Y. Zhao, J. Li, L. Chang, and W. Zhao, A green anti-solvent process for high performance carbon-based CsPbI<sub>2</sub>Br all-inorganic perovskite solar cell, *Sol. RRL* **2**, 1800139 (2018).
- [57] H. Dong, J. Xi, L. Zuo, J. Li, Y. Yang, D. Wang, Y. Yu, L. Ma, C. Ran, and W. Gao, Conjugated molecules “bridge”: Functional ligand toward highly efficient and long-term stable perovskite solar cell, *Adv. Funct. Mater.* **29**, 1808119 (2019).
- [58] B. Hailegnaw, N. S. Sariciftci, and M. C. Scharber, Impedance spectroscopy of perovskite solar cells: Studying the dynamics of charge carriers before and after continuous operation, *Phys. Status Solidi A* **217**, 2000291 (2020).
- [59] Y. Li, Z. Xu, S. Zhao, B. Qiao, D. Huang, L. Zhao, J. Zhao, P. Weng, Y. Zhu, and X. Li, Highly efficient p-i-n perovskite solar cells utilizing novel Low-temperature solution-processed hole transport materials with linear  $\pi$ -conjugated structure, *Small* **12**, 4902 (2016).
- [60] D. Prochowicz, M. M. Tavakoli, A. Kalam, R. D. Chavan, S. Trivedi, M. Kumar, and P. Yadav, Influence of A-site cations on the open-circuit voltage of efficient perovskite solar cells: A case of rubidium and guanidinium additives, *J. Mater. Chem. A* **7**, 8218 (2019).
- [61] W. S. Subhani, K. Wang, M. Du, X. Wang, and S. Liu, Interface-modification-induced gradient energy band for highly efficient CsPbI<sub>2</sub>Br<sub>2</sub> perovskite solar cells, *Adv. Energy Mater.* **9**, 1803785 (2019).
- [62] G. Yang, C. Wang, H. Lei, X. Zheng, P. Qin, L. Xiong, X. Zhao, Y. Yan, and G. Fang, Interface engineering in planar perovskite solar cells: Energy level alignment, perovskite morphology control and high performance achievement, *J. Mater. Chem. A* **5**, 1658 (2017).
- [63] S. Yang, W. Liu, Y. Han, Z. Liu, W. Zhao, C. Duan, Y. Che, H. Gu, Y. Li, and S. Liu, 2D Cs<sub>2</sub>PbI<sub>2</sub>Cl<sub>2</sub> nanosheets for holistic passivation of inorganic CsPbI<sub>2</sub>Br perovskite solar cells for improved efficiency and stability, *Adv. Energy Mater.* **10**, 2002882 (2020).
- [64] J. Zhang, D. Bai, Z. Jin, H. Bian, K. Wang, J. Sun, Q. Wang, and S. Liu, 3D–2D–0D interface profiling for record efficiency all-inorganic CsPbBr<sub>2</sub> perovskite solar cells with superior stability, *Adv. Energy Mater.* **8**, 1703246 (2018).
- [65] H. Zhao, Y. Han, Z. Xu, C. Duan, S. Yang, S. Yuan, Z. Yang, Z. Liu, and S. Liu, A novel anion doping for stable CsPbI<sub>2</sub>Br perovskite solar cells with an efficiency of 15.56% and an open circuit voltage of 1.30V, *Adv. Energy Mater.* **9**, 1902279 (2019).
- [66] Y.-W. Jang, S. Lee, K. M. Yeom, K. Jeong, K. Choi, M. Choi, and J. H. Noh, Intact 2D/3D halide junction perovskite solar cells via solid-phase In-plane growth, *Nat. Energy* **6**, 63 (2021).
- [67] X. Li, W. Zhang, X. Guo, C. Lu, J. Wei, and J. Fang, Constructing heterojunctions by surface sulfidation for efficient inverted perovskite solar cells, *Science* **375**, 434 (2022).
- [68] Z. Ni, C. Bao, Y. Liu, Q. Jiang, W.-Q. Wu, S. Chen, X. Dai, B. Chen, B. Hartweg, Z. Yu, *et al.*, Resolving spatial and energetic distributions of trap states in metal halide perovskite solar cells, *Science* **367**, 1352 (2020).
- [69] L. McGovern, I. Koschany, G. Grimaldi, L. A. Muscarella, and B. Ehrler, Grain size influences activation energy and migration pathways in MAPbBr<sub>3</sub> perovskite solar cells, *J. Phys. Chem. Lett.* **12**, 2423 (2021).
- [70] W. Peng, L. Wang, B. Murali, K.-T. Ho, A. Bera, N. Cho, C.-F. Kang, V. M. Burlakov, J. Pan, and L. Sinatra, Solution-grown monocrystalline hybrid perovskite films for hole-transporter-free solar cells, *Adv. Mater.* **28**, 3383 (2016).
- [71] D. Abou-Ras, T. Kirchartz, and U. Rau, *Advanced Characterization Techniques for Thin Film Solar Cells* (Wiley Online Library, Weinheim, 2011), Vol. 2, Chapter 4.
- [72] J. Siekmann, S. Ravishankar, and T. Kirchartz, Apparent defect densities in halide perovskite thin films and single crystals, *ACS Energy Lett.* **6**, 3244 (2021).
- [73] F. Werner and S. Siebentritt, Buffer Layers, Defects, and the Capacitance Step in the Admittance Spectrum of a Thin-Film Solar Cell, *Phys. Rev. Appl.* **9**, 054047 (2018).
- [74] T. Eisenbarth, T. Unold, R. Caballero, C. A. Kaufmann, and H.-W. Schock, Interpretation of admittance, capacitance-voltage, and current-voltage signatures in Cu(In,Ga)Se<sub>2</sub> thin film solar cells, *J. Appl. Phys.* **107**, 034509 (2010).
- [75] I. Zarazua, G. Han, P. P. Boix, S. Mhaisalkar, F. Fabregat-Santiago, I. Mora-Seró, J. Bisquert, and G. Garcia-Belmonte, Surface recombination and collection efficiency in perovskite solar cells from impedance analysis, *J. Phys. Chem. Lett.* **7**, 5105 (2016).
- [76] D. A. Jacobs, H. Shen, F. Pfeffer, J. Peng, T. P. White, F. J. Beck, and K. R. Catchpole, The two faces of capacitance: New interpretations for electrical impedance measurements of perovskite solar cells and their relation to hysteresis, *J. Appl. Phys.* **124**, 225702 (2018).
- [77] S. Ravishankar, C. Aranda, S. Sanchez, J. Bisquert, M. Saliba, and G. Garcia-Belmonte, Perovskite solar cell modeling using light-and voltage-modulated techniques, *J. Phys. Chem. C* **123**, 6444 (2019).
- [78] D. Moia, I. Gelmetti, P. Calado, W. Fisher, M. Stringer, O. Game, Y. Hu, P. Docampo, D. Lidzey, and E. Palomares, Ionic-to-Electronic current amplification in hybrid perovskite solar cells: Ionically gated transistor-interface circuit model explains hysteresis and impedance of mixed conducting devices, *Energy Environ. Sci.* **12**, 1296 (2019).
- [79] F. Ebadi, N. Taghavinia, R. Mohammadpour, A. Hagfeldt, and W. Tress, Origin of apparent light-enhanced and negative capacitance in perovskite solar cells, *Nat. Commun.* **10**, 1 (2019).
- [80] S. Ravishankar, M. Garcia-Battle, J. Bisquert, G. Garcia-Belmonte, J. Odobina, and C.-A. Schiller, Removing

- instability-caused low-frequency features in small perturbation spectra of perovskite solar cells, *J. Phys. Chem. C* **124**, 15793 (2020).
- [81] W. Peng, C. Aranda, O. M. Bakr, G. Garcia-Belmonte, J. Bisquert, and A. Guerrero, Quantification of ionic diffusion in lead halide perovskite single crystals, *ACS Energy Lett.* **3**, 1477 (2018).
- [82] J. H. Scofield, Effects of series resistance and inductance on solar cell admittance measurements, *Sol. Energy Mater. Sol. Cells* **37**, 217 (1995).
- [83] D. Losee, Admittance spectroscopy of impurity levels in Schottky barriers, *J. Appl. Phys.* **46**, 2204 (1975).
- [84] J. Kneisel, K. Siemer, I. Luck, and D. Bräunig, Admittance spectroscopy of efficient CuInS<sub>2</sub> thin film solar cells, *J. Appl. Phys.* **88**, 5474 (2000).
- [85] N. D. Nguyen, M. Germain, M. Schmeits, B. Schineller, and M. Heuken, Thermal admittance spectroscopy of Mg-doped GaN Schottky diodes, *J. Appl. Phys.* **90**, 985 (2001).
- [86] M. Burgelman and P. Nollet, Admittance spectroscopy of thin film solar cells, *Solid State Ion.* **176**, 2171 (2005).
- [87] A. Gudovskikh, J.-P. Kleider, J. Damon-Lacoste, P. R. i Cabarrocas, Y. Veschetti, J.-C. Muller, P.-J. Ribeyron, and E. Rolland, Interface properties of a-Si: H/c-Si heterojunction solar cells from admittance spectroscopy, *Thin Solid Films* **511**, 385 (2006).
- [88] R. A. Awni, Z. Song, C. Chen, C. Li, C. Wang, M. A. Razzoqi, L. Chen, X. Wang, R. J. Ellingson, and J. V. Li, Influence of charge transport layers on capacitance measured in halide perovskite solar cells, *Joule* **4**, 644 (2020).
- [89] M. Samiee, S. Konduri, B. Ganapathy, R. Kottokkaran, H. A. Abbas, A. Kitahara, P. Joshi, L. Ziang, M. Noack, and V. Dalal, Defect density and dielectric constant in perovskite solar cells, *Appl. Phys. Lett.* **105**, 153502 (2014).
- [90] H.-S. Duan, H. Zhou, Q. Chen, P. Sun, S. Luo, T.-B. Song, B. Bob, and Y. Yang, The identification and characterization of defect states in hybrid organic-inorganic perovskite photovoltaics, *Phys. Chem. Chem. Phys.* **17**, 112 (2015).
- [91] Q. Chen, H. Zhou, Y. Fang, A. Z. Stieg, T.-B. Song, H.-H. Wang, X. Xu, Y. Liu, S. Lu, and J. You, The optoelectronic role of chlorine in CH<sub>3</sub>NH<sub>3</sub>PbI<sub>3</sub>(Cl)-based perovskite solar cells, *Nat. Commun.* **6**, 1 (2015).
- [92] S. H. Cho, J. Byeon, K. Jeong, J. Hwang, H. Lee, J. Jang, J. Lee, T. Kim, K. Kim, M. Choi, *et al.*, Investigation of defect-tolerant perovskite solar cells with long-term stability via controlling the self-doping effect, *Adv. Energy Mater.* **11**, 2100555 (2021).
- [93] Q. Dong, C. H. Y. Ho, H. Yu, A. Salehi, and F. So, Defect passivation by fullerene derivative in perovskite solar cells with aluminum-doped zinc oxide as electron transporting layer, *Chem. Mater.* **31**, 6833 (2019).
- [94] O. Almora, M. Garcia-Batlle, and G. Garcia-Belmonte, Utilization of temperature-sweeping capacitive techniques to evaluate band gap defect densities in photovoltaic perovskites, *J. Phys. Chem. Lett.* **10**, 3661 (2019).
- [95] Scripts for all MATLAB, SCAPS, and SETFOS simulations in this work are deposited in the Zenodo archive with the following identifier: <https://doi.org/10.5281/zenodo.6114624>.